Coastal Engineering 199 (2025) 104739

Contents lists available at ScienceDirect

Coastal Engineering

journal homepage: www.elsevier.com/locate/coastaleng

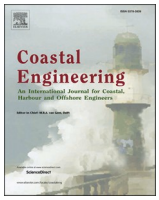

Submerged and emerged rigid vegetation impact on bedforms and sediment suspension under wave action

K. Ions [a], X. Wang [a], D.E. Reeve [a], N. Mori [b,c,d], H. Karunarathna [a,*]

[a] Faculty of Science and Engineering, Swansea University, Swansea, United Kingdom
[b] Honorary Professor, Faculty of Science and Engineering, Swansea University, Swansea, United Kingdom
[c] Disaster Prevention Research Institute, Kyoto University, Kyoto, Japan
[d] Typhoon Research Center, Yokohama National University, Japan

A B S T R A C T

A series of experiments were carried out in a laboratory wave flume to investigate the impact of coastal rigid vegetation on suspended sediment transport and the generation of bedforms for a range of wave conditions for both submerged and emerged vegetations. Rigid arrays of cylindrical wooden dowels were used as vegetation mimics on a sandy bed. Two vegetation densities were selected, representing dense and sparse vegetation meadows. Synchronised flow velocity and suspended sediment concentration measurements were performed using particle image velocimetry and an acoustic backscatter sensor. Seabed ripples were observed in all cases where the near-bed velocity exceeded the threshold of sediment motion. The near-bed velocity governed sediment suspension on both bare and vegetated sediment seabeds. Near-bed sediment concentration on densely vegetated seabeds was lower than that of bare seabeds under the same wave conditions. These observations highlight the importance of considering the role of vegetation in shaping seabed morphology and the resultant suspended sediment concentrations. Then, the near-bed sediment concentration formulae used on bare sediment beds are validated for use on vegetated seabeds.

1. Introduction

Coastal regions are prone to extreme storms and rising sea levels, a combination of which may enhance the erosion of sandy beaches (Vousdoukas et al., 2020; Luijendijk et al., 2018; Ranasinghe, 2016; Kirezci et al., 2020). At the same time, the global population living near coastal regions is expected to continue to rise (Hugo, 2011; Reimann et al., 2023). This is due to the wide range of economic, social, and health benefits coastal regions provide (Wheeler et al., 2012; UK Government, 2021). To adapt to climate change impacts on the coastal environment such as increasing coastal erosion and flooding, and the pressures of the ever-growing coastal population, a myriad of options must be considered. One option that has recently gained global traction is Nature-based Solutions (NbS) involving natural coastal ecosystems such as saltmarshes, mangroves, and seagrass beds (Seddon et al., 2020; Narayan et al., 2016; Sutton-Grier et al., 2015; Pontee et al., 2016) into engineering solutions (Menéndez et al., 2020; Fairchild et al., 2021; Gracia et al., 2018; Ondiviela et al., 2014).

Coastal vegetation is found globally in intertidal zones (Bouma et al., 2005). Often, they can be found in sheltered, low-energy environments (McOwen et al., 2017; Giri et al., 2011). They have been proven to attenuate wave energy and flow velocity (Yang, 1998; Koch and Gust, 1999; Gambi et al., 1990; Möller et al., 2014), reduce coastal erosion, and promote sediment deposition (Kathiresan, 2003; Horppila and Nurminen, 2003; Zhu et al., 2015; Reidenbach and Timmerman, 2019; Furukawa et al., 1997). In turn, this increases bed elevation (McKee et al., 2007; McKee, 2011; Furukawa et al., 1997) and can significantly increase water quality (Green and Short, 2003; Fourqurean et al., 2012). An increase in sediment deposition and bed elevation is identified as one major strength of vegetation as an NbS. The adaptability of NbS against rising sea levels presents them as more sustainable coast protection measures with greater resilience against climate change (Moritsch et al., 2022; Fagherazzi et al., 2017, 2020; McKee et al., 2007). The economic impact of coastal vegetation as a natural buffer zone has been found to reduce flood damage costs by up to 37% across large salt marsh estuaries (Barbier et al., 2011). The benefits of coastal vegetation extend beyond an engineering standpoint, as these species play a pivotal role in shaping their environment, conserving local ecology, providing numerous ecosystem services, and benefiting local economies (Temmerman et al., 2013; Himes-Cornell et al., 2018).

Significant advances have been made in understanding the impacts of coastal vegetation on wave hydrodynamics through field studies (Mazda et al., 2006; Möller, 2006; Möller et al., 2014; Quartel et al., 2007; Jadhav et al., 2013) and laboratory investigations (Losada et al.,

* Corresponding author.
E-mail address: h.u.karunarathna@swansea.ac.uk (H. Karunarathna).

https://doi.org/10.1016/j.coastaleng.2025.104739
Received 19 November 2024; Received in revised form 28 February 2025; Accepted 28 February 2025
Available online 5 March 2025

2016; Hu et al., 2014; Kobayashi et al., 1993; van Veelen et al., 2020; Maza et al., 2015; Ozeren et al., 2014; Koftis et al., 2013; Anderson and Smith, 2014). However, the land-sea interface of coastal ecosystems is also linked with transporting sediment (Ward et al., 2020). Therefore, if NbS are to be implemented, the feedback system between hydrodynamics, sediment, and vegetation must be better understood.

Decades of research have been carried out on sediment transport on bare sandy beds (Fredsøe and Deigaard, 1992; Nielsen, 1992; Van Veelen et al., 2020, b, c; Green and Coco, 2014) which have led to significant advances in knowledge. However, studies utilising full-scale and laboratory-scale experiments have highlighted the complex nature of sediment transport amongst coastal vegetation. The scale at which vegetation-sediment interaction is considered appears to dictate the process somewhat. In the interior regions of coastal vegetation, wave attenuation is significant, acting over tens of metres to kilometres. This large wave attenuation can sometimes limit near-bed velocity where sediment threshold motion is often not exceeded (e.g., Reidenbach and Thomas, 2018). Multiple studies have reported a reduction in suspended sediment concentration (*SSC*), and near-bed velocity on most vegetation meadows with sufficient plant density and area coverage in the field (Horppila and Nurminen, 2003; Zhu et al., 2015; Reidenbach and Timmerman, 2019; Leonard and Croft, 2006; Neumeier and Amos, 2006; Chen et al., 2018).

In contrast, enhanced sediment suspension has been observed in areas of insufficient vegetation densities (Hansen and Reidenbach, 2013). Additionally, decreased sediment deposition has been observed at the edge of mangrove forests where flow velocity is high (Horstman et al., 2014). A series of field studies carried out on mangrove pneumatophores have found increased turbulence levels generated by the vegetation stems, which can lead to increased *SSC* or decreased sediment deposition relative to bare sediment beds (Norris et al., 2017, 2019, 2021). Mullarney et al. (2017) observed scouring around individual pneumatophores in the field. These field studies provide insights into the complex feedback between sediment, hydrodynamics, and vegetation. Gillis et al. (2022) also found that the rigid vegetation is crucial for buffering hydrodynamics, and may increase erosion within the frontal vegetation meadow and lateral edges. To better understand the feedback between sediment and vegetation, laboratory studies have focused on small-scale interactions ranging from a few millimetres to several metres. There is a growing body of literature which supports field observations on vegetation-enhancing sediment suspension relative to bare flat sediment beds under the same wave conditions for particular conditions (Yang et al., 2016; Tinoco and Coco, 2014; Tinoco and Coco, 2018; Tang et al., 2019; Lou et al., 2022; Ros et al., 2014; Marin-Diaz et al., 2020; Lou et al., 2022).

Whilst these studies have now resolved some differences found on sediment suspension and sediment deposition observed at stem-scale interaction, the focus has been on suspension over flat sediment beds. In nature, seabed bathymetry is often complex, and ripples are known to form on sandy beds when near-bed wave velocity magnitudes are sufficiently strong to move seabed sediment (Inman, 1957; Miller & Komar, 1980). It has been shown that the near-bed turbulent structures and sediment suspension process differ on rippled beds when compared with flat beds. The formation of ripples enhances bottom roughness, thus increasing wave dissipation from bottom friction (Brevik and Bjørn, 1979; Mathisen and Madsen, 1996; Fredsøe and Deigaard, 1992) thus impacting sediment mobility (Green and Black, 1999; Williams and Kemp, 1971; Nielsen, 1986). Such ripples have been observed also amongst coastal vegetation (Mullarney et al., 2017; Norris et al., 2021).

Ripples are characterised by the ripple wavelength (λ_r), defined as the distance between two ripple crests, and ripple height (η_r), defined as the vertical distance from the ripple trough to the ripple crest (Appendix A – Fig. A1). When ripples are sufficiently steep, i.e., when $\eta_r/\lambda_r > 0.12$, vortices form closer to the ripple crest (Davies and Villaret, 1999; Thorne et al., 2002; Thorne et al., 2009). Upon flow reversal, these vortices are ejected upwards on the lee side of the ripple. These vortices carry substantial amounts of sediment upwards into the water column. Due to the regular, symmetric pattern of the bed that typically forms under oscillatory flows, the vortices provide a constant, coherent turbulence structure (Thorne et al., 2009). Thorne et al. (2002, 2009) showed that this manifests as a constant sediment diffusivity, typically occurring at heights of 3–4 times the ripple crest height, above the ripple crest (Thorne et al., 2009). Turbulence becomes increasingly random outside this region, and sediment diffusivity increases linearly over the bed (Nielsen, 1992; Thorne et al., 2002). Once wave conditions exceed a certain threshold, sheet flow conditions develop, and ripples are washed out. Davies and Villaret (2002) highlighted the paradoxical nature by which lower wave conditions generate steeper ripples, thus increasing the *SSC* in the water column.

In the near bed layer of sediment over ripple beds, there is a notable difference in momentum transfer and an increase in bottom roughness (k_b) compared to flat beds with no ripples. Zhang and Nepf (2019) first researched the effects of flexible plant mimics with a rigid sheath on ripple formation and the resulting sediment suspension on a sand seabed in a laboratory wave flume. They observed that the enhanced turbulence within the vegetation mimics contributed to a faster ripple formation than a bare sediment bed. It was shown that the non-vegetated cases had comparable suspension concentrations to vegetated cases. Additionally, when wave orbital excursion (A_w) was larger than the spacing between stems in the direction of wave propagation (S_x), the stem-generated turbulence was sufficiently large to remove sediment from ripples and the bed was returned to a flatbed. It is, therefore, reasonable to expect that, under viable conditions, ripples will form on vegetated seabeds and that their impact on sediment transport on sediment transport should not be neglected.

With an increasing focus on NbS for coastal protection and coastal wetland restoration efforts, the role of vegetation on sediment suspension compared to bare sediment beds must be fully understood to make informed management decisions. The role of vegetation array density must be further studied to quantify conditions where ripple formation is possible within vegetation canopies. In this study, we seek to explore the impacts of rigid vegetation on ripple formation and suspended sediment transport within vegetation meadows, through an experimental study in a laboratory wave flume. Section 2 describes the background literature and theory relevant to this study. Section 3 gives a detailed description of the experimental methods used and the methods of analysis. Section 4 presents our experimental observations, starting with the formation of ripples, followed by near-bed-hydrodynamics and near-bed sediment concentration. Section 5 provides in-depth discussions on the three aspects of Section 4. Finally, Section 6 concludes the paper.

2. Theoretical background

There are predominately three types of ripples formed on sandy sea beds: orbital-ripples, which form under smaller values of A_w/D_{50}, typically < 2000. Here, $\lambda_r \propto D_{50}$, in which D_{50} is the median sediment size and $A_w = \frac{U_{w,bed}T}{2}$ in which $U_{w,bed}$ is the maximum velocity in the near-bed area (the area around 4 to 5 times of η_r above ripple crest (Thorne et al., 2003)); anorbital ripples which form for reasonably large values of A_w/D_{50}, typically > 5000 and λ_r is approximately equal to $500D_{50}$; and sub-orbital ripples which form when both orbital and sub-orbital ripples are possible (Clifton, 1976). Our study is predominantly focused on orbital ripples. Following the methodology of Thorne et al. (2002), ripples are considered steep enough to form vortices and resuspend sediment if $\eta_r/\lambda_r > 0.12$. If no ripples are present or $\eta_r/\lambda_r < 0.12$, then those cases are considered flatbed cases.

Numerous studies have reported *SSC* over sandy, rippled beds under wave motion (Fredsøe and Deigaard, 1992; Nielsen, 1992; van Rijn et al., 1993, 2007; Thorne et al., 2002, 2009). *SSC* has been defined using two attributes in the literature: (i) The *SSC* profile over the water column (where depth is 0 at the free water surface and increases towards

the bed, denoted by Z); and (ii) $C0$, which was taken at some distance Z_{ref} above the bed. Throughout the literature, the 'near bed' location of $C0$ varies depending on the practical limitation of the study concerned. For rippled beds, the reference height should be close to the location of the ripple crest.

The SSC at any given water depth is described by

$$C(z) = C_0\Phi(Z) \tag{1}$$

where Φ is a shape function that describes the SSC profile shape. In this study, Nielsen's 1992 formulation for Φ is considered,

$$\Phi = \left(1 + \frac{Z}{Z_1}\right)^{-\xi} \tag{2}$$

Z is measured from the bed, starting at $Z = 0$ m and Z_1 is the maximum vertical distance from the bed by which the ripple-generated sediment is moved upwards in the water column, $Z_1 = 0.09\sqrt{k_b A_w}$.The definition of k_b is given as $k_b = \delta\eta_r^2/\lambda_r$, δ was calibrated by Nielsen (1992) as $\delta = 8$ and by Thorne et al. (2009) as $\delta = 25$. ξ is an empirical coefficient which governs the shape of the SSC profile, typically $\xi = 2$.

Nielsen's (1986) was used to calculate $C0$ in this study. This equation was selected for two reasons: firstly, the method was derived for use, especially on rippled sediment beds. Secondly, several studies have highlighted the strength and applicability of this equation (Green and Black, 1999; Thorne et al., 2002; Goldstein et al., 2013). According to their equation, $C0$ is defined as

$$C0 = \gamma\rho_s\theta_r^3 \tag{3}$$

θ_r is the modified shields parameter over rippled beds accounts for flow enhancement over a ripple crest. γ, is a calibrated coefficient ranging from 0.0022 to 0.005 (Nielsen, 1986; Thorne et al., 2002), and ρ_s is the sediment density. Nielsen (1986) implemented Du Toit and Sleath (1981) maximum near-bed velocity over rippled bed solution into existing shields parameter. θ_r is expressed

$$\theta_r = \frac{\theta'}{\left(1 - \frac{\pi\eta_r}{\lambda_r}\right)^2} \tag{4}$$

in which η_r and λ_r are ripple crest height and ripple length, respectively (see Appendix A – Fig. A1 for further details). θ' is the traditional shield parameter over flat beds, expressed as

$$\theta' = \frac{f_w\Psi}{2} \tag{5}$$

Ψ is the wave mobility number, which is expressed as

$$\Psi = \frac{A_w^2\omega^2}{(s-1)gD_{50}} \tag{6}$$

ω is the angular frequency of the wave, s is the relative density of sediment $(p_s - p)/p_s$, g is the acceleration due to gravity.

The wave friction factor (skin friction) f_w which was derived by Swart (1974) can be expressed as

$$f_w = \exp\left[5.213\left(\frac{2.5D_{50}}{A_w}\right)^{0.194} - 5.977\right] \tag{7}$$

In all cases, the maximum velocity at the bed, $U_{w,bed}$ was greater than U_{thresh}, which was defined using Komar and Miller (1973) in Eq. (8).

$$\frac{\rho U_{thresh}^2}{(\rho_s - \rho)gD_{50}} = 0.30\left(\frac{2A_w}{D_{50}}\right)^{0.5}. \tag{8}$$

Under the same wave conditions, the above equations were calibrated firstly on the bare sediment bed and then on sediment beds with dense and sparse rigid vegetation cases. Drawing comparisons between the experimental cases under the same initial wave conditions will reveal the impact of rigid vegetation and the density of rigid vegetation on ripple formation and sediment suspension within vegetation canopies.

3. Methodology

The experiments were conducted in a 30.7 m long, 0.8 m wide, and 1.2 m deep wave flume in the Coastal Engineering Laboratory of Swansea University, UK. The flume has a piston-type wave generator with regular and random wave generation capabilities, glass side walls, and a metal bottom. A parabolic wave absorber, made from reticulated foam, is located at the opposite end of the wave generator (Fig. 1).

3.1. Experimental set-up

The model vegetation mimics were secured to perforated aluminium sheets fastened to the flume bottom. Each sheet was 0.5 m long × 0.8 m wide and 0.9 mm thick. The model rigid vegetation comprised of cylindrical, rigid bamboo dowels, with $EI = 9 \pm 4 \times 10^{-2}$ Nm^2. The stem height (h_v) and diameter (b_v) were 0.3 m and 5 mm, respectively. The 4.5 m long vegetation meadow was formed by putting together nine aluminium sheets with vegetation mimics started at a distance of 9.8 m and extended to 14.3 m away from the home position of the wave paddle. The length of the meadow was selected to be larger than the largest wavelength (3.44 m) used in the experiments. There was a 10 cm window without vegetation in the vegetation meadow, for the purpose of hydrodynamic measurements. Two vegetation densities were selected: $N_v = 85$ and $N_v = 350$ stems/m^2, corresponding to ah= 0.106 and 0.438, respectively, where a is the volumetric frontal area of the stem. These values are representative of dense ($N_v = 350$) and sparse ($N_v = 85$) array densities ($ah < 0.1$ for sparse arrays and $ah > 0.1$ for dense arrays) (Nepf, 2012) found in nature.

The model vegetation stems are representative of nature in which vegetation diameters vary from a few mm for saltmarsh or seagrass species (*Spartina anglica*, *Spartina alterniflora* and *Zostera Marina*, Bennett et al., 2020; Vuik et al., 2018; Hansen and Reidenbach, 2012). The array configuration and stem densities were also selected to ensure a wide range of A_w/S_x values (0.25–1.35) to be covered and to draw comparisons with findings from previous experimental studies (e.g., Zhang and Nepf, 2019). S_x was taken as 6 cm for dense vegetation and 12 cm for sparse vegetation (Fig. 1). The lateral spacing of stems across the width of the flume, S_y was 8 cm for dense vegetation and 16 cm for sparse vegetation (Fig. 1).

A 5 cm layer of sediment is placed over the vegetation meadow. Therefore the stem height, $h_v = 0.25$ cm above the sandybed. The sediment layer extended 1 m at both sides of the vegetation meadow, making a total of 6.5 m of sedimented seabed. The extended bare sandy bed represented natural conditions, where waves often propagate over bare sediment bed regions before interacting with vegetation. The sediment grain sizes were $D_{50} = 0.300$ μm, $D_{90} = 398$ μm, $D_{10} = 160$ μm and the density ρ_s was 2.64 g/cm^3. These values are representative of sediment found in nature, such as in seagrass beds and the fringes of saltmarshes and mangrove forests (Infantes et al., 2012; Masselink et al., 2024; Mullarney et al., 2017) and closely align with previous studies (Marin-Diaz et al., 2020; Tinoco and Coco, 2018; Thorne et al., 2002). To ensure the sediment was kept in the desired location, two metal slopes were secured to the flume bottom at either end of the sediment layer.

3.2. Hydrodynamic measurements

Laboratory experiments were conducted under a range of wave heights (H_s), wave periods (T) and two water depths (h). H_s varied between 0.06 and 0.2 m and T from 1.0 to 2.0 s at the wave paddle. Since the study aims to investigate sediment suspension, the wave heights and

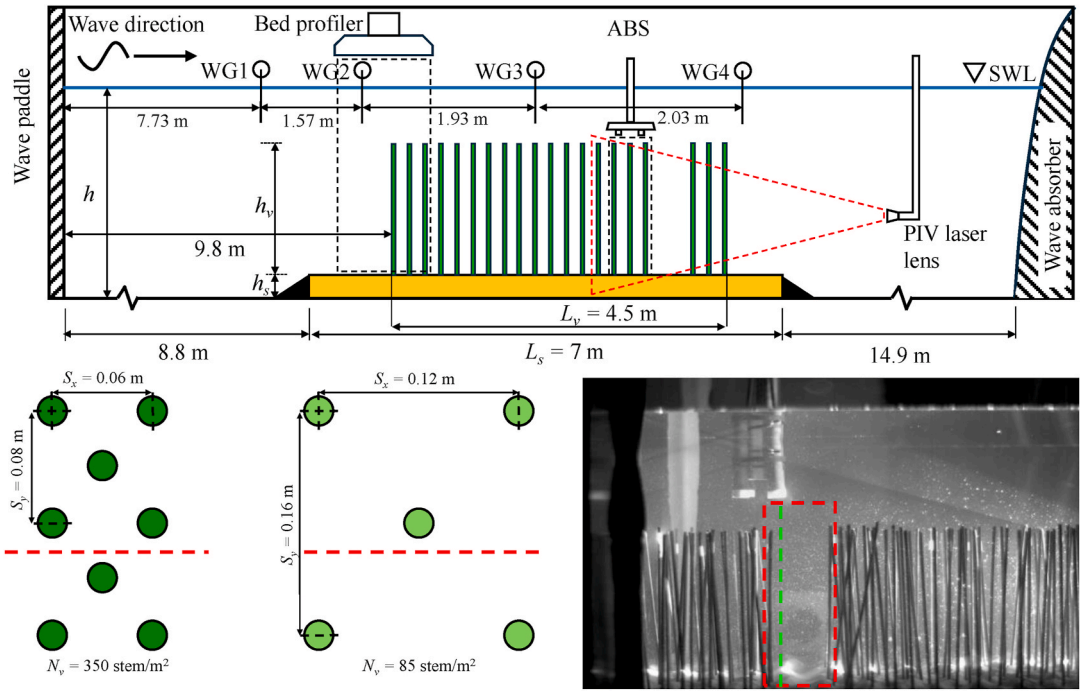

Fig. 1. Top: Experimental set-up in the wave flume at Swansea University. Bottom left: dense and sparse vegetation stem arrangement. The red dashed lines in the stem array diagrams represent the transect the PIV laser passes through. Bottom right: a sample image from PIV set-up for submerged rigid vegetation. The red rectangle represents the PIV measurement window free of stems and the dashed green line represents where ABS measurements were taken. (For interpretation of the references to colour in this figure legend, the reader is referred to the Web version of this article.)

wave periods were selected to give a range of maximum near-bed velocity values calculated based on linear wave theory. The two water depths were 0.3 m and 0.45 m, giving the depth of submergence of vegetation (h_v/h) of 1.0 and 0.66, where h_v is the vegetation stem height. Those parameters were combined to form 17 different hydrodynamic conditions (Appendix A1– Table A1). First, the bare sediment seabed (Fig. 1) was tested under those 17 hydrodynamic conditions, which acted as the reference conditions. Then, vegetation meadows with two different densities ('dense' array and 'sparse' array) were tested under the same hydrodynamic conditions. Those three sets of experiments formed 51 experiments in total.

Four wave gauges were deployed. WG1 was placed at the toe of the slope, WG2 at the start of the vegetation, WG3 midway through the vegetation meadow, and WG4 just after the vegetation meadow, as shown in Fig. 1. Taking the average H_s at WG4 ($\overline{H_{s\ at\ WG4}}$), the wave attenuation is quantified through $\frac{\overline{H_{s\ at\ WG4}}}{H_s}$, and can be found in Appendix A – Table A1.

The water particle velocities were measured using particle imagery velocimetry, PIV (Dantec Systems - Nano L 100-50, Litron Laser) at approximately 4.1 m downstream of the start of the vegetation meadow. Polyamide seeding particles with a diameter of 50 μm were used in PIV measurements. Adopting the approach used in previous similar experimental studies, a few rows of vegetation were removed from the vegetation meadow, creating a 10 cm measurement window between rows of stems as shown in Fig. 1 (e.g., Luhar et al., 2010; Pujol et al., 2013; Van Veelen et al., 2020; Tseng and Tinoco, 2021). This was done to ensure the measurements were not impacted by the direct interference of stems. It should be noted that the vegetation gap was set near the end of the vegetation meadow, to make sure wave attenuation, as well as turbulence generated by the stems and ripples will not be impacted. It has been proved that the velocity measured within the gap is representative of the velocity in the stem array (e.g. Tseng and Tinoco, 2021). The submerged PIV laser was fired towards the downstream of the flume. The exact vertical location of the laser was optimised for each water depth. The PIV laser was coupled with a high-speed camera at the lateral side of the flume. Images were captured by the camera at a rate of 50 Hz for 90 s. The relevant images were then selected so that no wave reflection was included in the measurements. This was achieved by initially calculating the return time of the reflected wave to reach WG4 (Möller et al., 2014). Accordingly, the water elevation time series were cropped to within 95% of the total. The transect used for velocity measurements is shown in the bottom panels of Fig. 1 as a box with dashed red line, while the transect for the ABS measuring is represented by a dashed green line.

The distance stem-generated turbulent kinetic energy (*TKE*) can travel before undergoing significant delay was shown to be equal to A_w on either side of the stem in the direction of wave propagation (Zhang et al., 2018). To address this, the transect used to extract velocity data at each depth was located within 2 cm of the last row of stems. However, the limitation of the PIV set-up and vegetation density is that the regions very close to the stem may not be captured, an issue also encountered by others (Zhang et al., 2018). Secondly, the selection of the transect in relation to the ripple crest or trough may influence the magnitude of *TKE* at the bed.

The post-processing of velocity data was carried out using the open-source PIVLab (Thielicke and Sonntag, 2021) with the following settings: Contrast Limited Adjustment Histogram Equalization (CLAHE) pixel size of 20 px; An image calibration factor of 1 px equal to 0.00064 m; The Fast Fourier transformation PIV settings were selected with four consecutive 50% size passes with 50% overlapped integration areas.

The PIV-derived velocity magnitudes provide a 2D vector field (shown in Appendix A, Fig. A2) separated into instantaneous horizontal, $U_i(x, z, t)$, and vertical, $V_i(x, z, t)$, velocity components. Each velocity component is decomposed into three parts. Then, the horizontal velocity, U_i can be written as

$$U_i = U_c + U_{w,rms} + u' \tag{9}$$

in which U_c is the mean current, $U_{w,rms}$ is the unsteady wave motion, and u' is the turbulent fluctuations. A similar decomposition is applied to the vertical component. The mean current (U_c) at each depth interval was

calculated by averaging the velocity over all wave periods, such that

$$U_c\,(z) = \frac{1}{2\pi}\int_0^{2\pi} U_i(\varphi)\,d\varphi, \tag{10}$$

in which, $U_i(\varphi)$ is the phase-dependent instantaneous velocity. The phase angle, $\varphi = |0 - 2\,\pi\,|$ and the number of phase bins, $\Delta\varphi = 2\pi/(TF)$, F = PIV sampling frequency, i.e., 50 Hz in this case (Tinoco and Coco, 2018). T he root mean square of the difference between $U_i(\varphi)$ and U_c , $U_{w,rms}(z)$, was calculated by phase-averaging the velocity in each phase bin and substracting U_c, to give the overall oscillatory variation of the flow, as seen in Equation (11).

$$U_{w,\mathrm{rms}}(z) = \sqrt{\frac{1}{2\pi}\int_0^{2\pi} (U_{i(\varphi)} - U_c)^2 d\theta} \tag{11}$$

The root mean square turbulent velocity fluctuations (u_{rms}, v_{rms}) for each time step were calculated as the deviation of instantaneous velocity from the phase averaged velocity in each bin. The set-up of PIV system offers only the vertical and horizontal decompositions of velocity. The two-component *TKE* analysis approach has been shown to be suitable (Tseng and Tinoco, 2021, 2022). The time-averaged, phase-averaged *TKE* at each depth interval is given in Equation (12).

$$TKE = \frac{1}{4\pi}\int_0^{2\pi} \left[2u_{rms}(\varphi)^2 + v_{rms}(\varphi)^2\right] d\varphi \tag{12}$$

For the present study, the classical definition of horizontal velocity amplitude at each depth interval is used for the comparison of velocities for different cases, which can be calculated as $U_w = \frac{U_{w,max} - U_{w,min}}{2}$, in which $U_{w,max}$, and $U_{w,min}$ were the maximum positive and negative velocities recorded at each elevation over the time series for the velocity data. The near-bed velocity is defined as $U_{w,bed}$ throughout the paper.

3.3. Experimental scaling

Adopting the previous methods for scaling of vegetation and wave conditions (Ghisalberti and Nepf, 2002; Luhar and Nepf, 2016; Luhar et al., 2017; Tang et al., 2019; van Veelen et al., 2020), the following non-dimensional parameters were identified to ensure the model conditions were representative of real-world conditions: kh (ratio of water depth to wave length); h_v/h (ratio of vegetation height to water depth); H/h (ratio of wave height to water depth); Froude number, $Fr = U_w/\sqrt{gh}$; the vegetation Reynolds number, $Re = U_w b_v/\nu$; Keulegan-Carpenter number, $KC_{stem} = U_w T/b_v$ (the ratio of wave excursion and stem diameter), which is a predictor for drag coefficients of cylinders. It is noted that the experimental parameters we adopted (see Appendix A – Table A1) are similar to Zhang and Nepf (2019) (see the Table 2 of Zhang and Nepf (2019)), which allows a comprehensive comparative study.

There are two primary forms of vegetation-induced turbulence: canopy-generated turbulence, TKE_{canopy} and stem-generated turbulence $TKE_{stem.}$ TKE_{canopy} is induced by the flow instability over the top of the canopy (Nepf, 2012) and is found during submerged vegetation conditions. Ghisalberti and Schlosser (2013) set out two conditions that must be satisfied to justify the presence of TKE_{canopy}. There is a temporal restraint of

$$KC_{canopy} = \frac{U_w T}{L_D} > 5 \tag{13}$$

L_D is the canopy drag length (Lowe et al., 2005), given by

$$L_D = \frac{(1-\lambda_p)}{CD\alpha} \tag{14}$$

λ_p is non-dimensional plant density and CD being the form drag and α is the vegetation submergence ratio (h_v/h). If $KC_{canopy} < 5$, there is insufficient time for the shearing levels required to cause flow instability on the top of the canopy. The second is a dynamic constraint,

$$Re_{canopy} = \frac{U_w^2 T}{2\pi\nu} > 1000 \tag{15}$$

Here, the fluid viscosity is sufficiently large for values less than 1 000 to prevent instability in the fluid. In this study, there were no cases of $KC_{canopy} > 5$, with maximum value for the fastest flow and densest cases $KC_{canopy} = 1.23$. Therefore, it is not expected that there will be any canopy-induced turbulence. Stem-generated turbulence is expected for all cases in the study (Appendix A – Table A1), with $KC_{stem} > 6$ (Sumer et al., 1997).

3.4. Sediment concentration and bed morphology measurements

Suspended sediment concentration (*SSC*) profiles were recorded simultaneously with the PIV velocity measurements using an Acoustic Backscatter Sensor (ABS). The ABS was located within the vegetation meadow, just upstream of the PIV window (Fig. 1). The location was selected by placing the ABS at three locations along the vegetation meadow and repeating the measurements at each location. The locations were: (i) far upstream of the PIV window, (ii) just before PIV window, and (iii) in the PIV window. The measurement at location (ii) was selected for analysis due to its proximity to the velocity measurement point and due to the fact that it is located within the vegetation meadow. Four frequency sensors of 0.5, 1.0, 2.0, and 4.0 MHz were installed, providing high spatial resolution (2.5 mm) and 100 Hz sampling frequency. The four frequency backscatter devices were secured together to a fixed position, creating a circular measurement area with a diameter of 5 cm. The sensors were consistently below the still water level, and their vertical position was adjusted to ensure the sensors were permanently submerged.

One key advantage of using ABS to measure suspended sediment over other methods is accurately identifying bed location; therefore, the *C0* value can be accurately derived from the data. The *SSC* profiles for each sensor were time-averaged and then averaged over all four sensors, to obtain the final *SSC* profile. A selection of sample mean *SSC* profiles on bare sediment bed, dense vegetation, and sparse vegetation are given in Appendix A – Fig. A3. The bed location was identified following the methods set out in Green and Black (1999) as follows: $\log_{10}$ *SSC* was plotted against the corresponding Z value, and the break-in slope was identified by fitting a straight line to the data. The break-in slope was then taken as bottom depth, Z_{ref}. The *C0* values were then taken at $SSC(Z_{ref})$. This was repeated for all cases to obtain the mean and uncertainty in all *SSC* and *C0* values. The error taken for $\overline{SSC}$ was the larger of the difference between $SSC(Z_{ref}+1)$ and $SSC(Z_{ref})$ and the difference between experimental repeats.

The ABS measurements, synchronised with the wave measurements, lasted 90 s. Given the short duration of those measurements, the *SSC* data for several cases were examined to ensure the stability of the measurements at each time interval for both repeats. This was repeated at three depth intervals (Z_{ref} and $Z = 2.5$ cm and $Z = 5$ cm). The *SSC* was found to stabilise during the time period where the water surface fluctuation is fully developed and stable. An example case portraying this is given in Fig. 2. The spatially averaged *SSC* time series data at Z_{ref} is plotted with the surface elevation time series at WG4 in Fig. 2. The stable interval before the arrival of the reflected wave, indicated by the green line, is used to calculate the time-averaged value of *SSC*. After this, the wave reflection is evident, and measurements beyond this interval were excluded from the analysis.

A seabed profiler (HR-Wallingford HRBP-1070) was deployed (Fig. 1) to capture the three-dimensional seabed morphology. For a selection of experimental runs, the bed profiler captured the bare and vegetated sandy seabed morphology, covering the region 0.5 m upstream to 0.5 m downstream of the start of the vegetation meadow, as shown in Fig. 1. The bed profiler had an accuracy of ±0.5 mm, with a

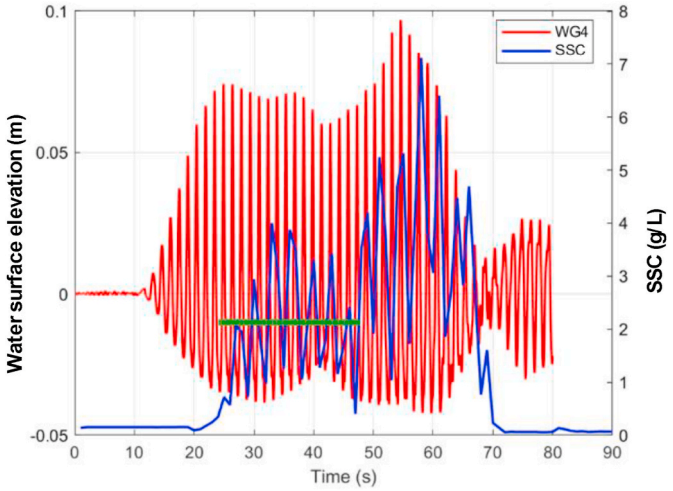

Fig. 2. Time series of SSC and surface elevation data at WG4. SSC data taken at Zref.

sampling frequency of 25 Hz. The transects were selected to extract the bed profile elevations for comparison (Fig. 3). The profiler data was used only to visually compare the role of stem-generated *TKE* in ripple formations.

The experimental schedule is generalised as follows: First, waves were run for 15 mins for each experimental condition, allowing any bedforms to generate and stabilise. Then, the water surface and the suspended sediment were allowed to settle until the ABS measurements were the same as the background value with no waves (0.002 g/L). Once settled, the same wave conditions were repeated for 1 min, during which waves, particle velocities, and suspended sediment concentrations were recorded at the measuring window shown in Fig. 1. After each experimental run, the bed was manually flattened using a high-pressured hosepipe in sweeping motions. Experiments were repeated twice. Visual observation and bed-profiler measurements confirm the formation of ripples for all experimental cases, excluding B1, B2, B10, DV1, DV2, DV10, DV11, DV13, and SV1 SV2, SV10 (Appendix A – Table A1), where the bed remained relatively flat. Those cases are excluded from the sediment suspension and *TKE* production analyses at the bed. Scour holes were visible when KC > 6, as Sumer et al. (1997) defined for vortex generation around cylindrical stems. The ripple dimensions can be viewed in Appendix A - Table 1.

4. Results

4.1. Ripple formation on vegetated seabeds

In general, once the ripples are formed, ripples alter the near-bed hydrodynamics, thus enhancing flow over the ripple crest (Nielsen, 1986). The ripples resuspended large quantities of sediment through vortex shedding, which enhances sediment suspension and *SSC* relative to plane beds (Sleath and Wallbridge, 2002; Davies and Villaret, 2002). As it is expected that vegetation stems interfere with this complex sediment dynamics, the impact of vegetation on ripple formation must be investigated to understand suspended sediment transport and seabed stability among vegetation canopies. For this purpose, the spatial characteristics of wave-induced ripples between the bare sediment bed region before the leading edge of the array and within the array, captured by the seabed profiler, are first analysed.

Bed profiler measurements of three experimental cases were selected for this analysis, highlighting the role of array spacing and A_w on ripple formation: (a) an emerged, sparse vegetation case (SV7, $A_w/S_x = 0.33$);

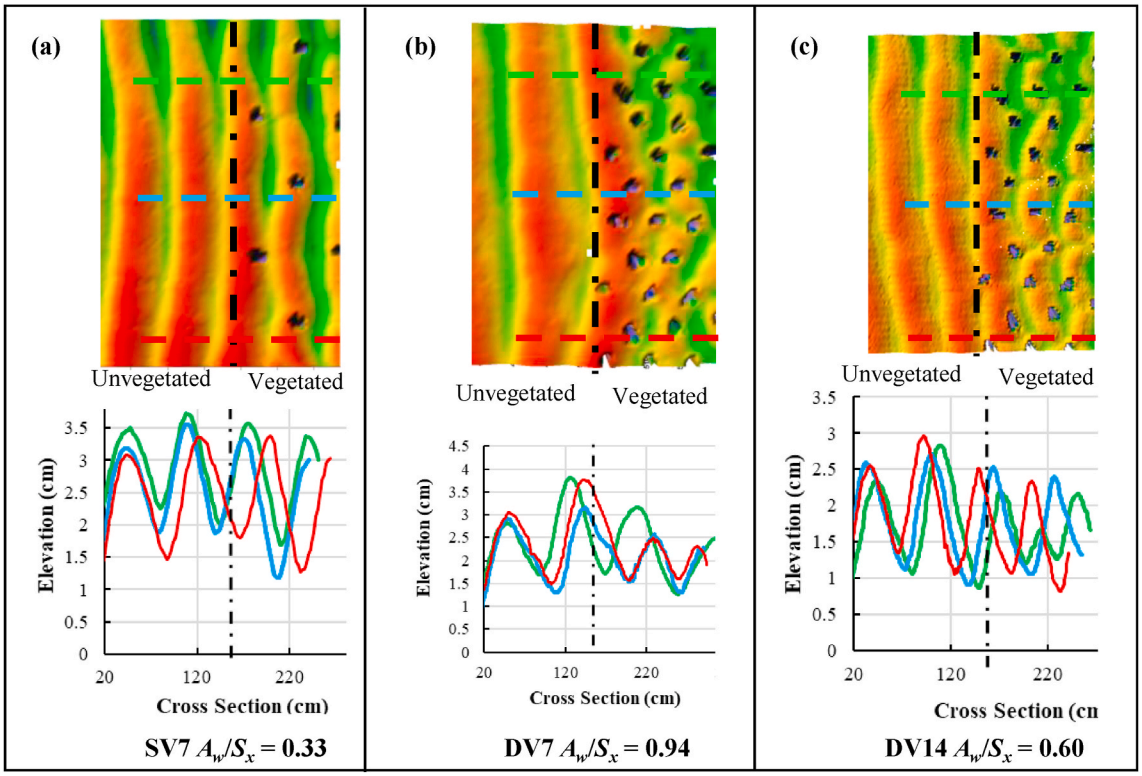

Fig. 3. Bed profile surveys covering bare sediment bed and vegetated bed. Black points indicate stem locations. Waves propagated from left to right. In the 1st row, the three dashed lines on each profile are the transects used to take ripple dimensions shown in the 2nd row. The vertical dot-dashed black line indicates the start of the vegetation meadow.

(b) an emerged, dense vegetation case under the same hydrodynamic conditions (DV7, $A_w/S_x = 1.06$); and (c) a submerged, dense vegetation case (DV14, $A_w/S_x = 0.60$). The ripples formed in these three cases and recorded by the bed profiler are presented in Fig. 3(a), (b) and (c), respectively. According to Fig. 3, it can be seen that the sediment at the immediate vicinity of the individual stems is removed, especially directly behind the stems, in all three cases. This phenomenon is much less significant in the cases of sparse vegetation, where well-structured, parallel ripples can be seen on both bare beds and vegetated areas (Fig. 3 (a)). Ripple dimensions on both vegetated and bare sediment bed areas are very similar. In contrast, the two dense vegetation cases show significant disruption to the ripple structure in the vegetated area, and the average dimensions of the remaining ripples in the vegetated area were smaller than those on the bare sediment bed area. In the emerged, dense vegetation case under the same hydrodynamic conditions (DV7- $A_w/S_x = 1.06$) (Fig. 3(b)), a significant disruption to the ripple structure can be seen in the vegetated area. Sediment is removed from the immediate vicinity of the individual stems, resulting in a more irregular ripple pattern. The average dimensions of the remaining ripples in the vegetated area were smaller than that of the bare bed area. It should be noted that DV7 has one of the largest A_w/S_x ratios. In the submerged, dense vegetation case (DV14 - Aw/Sx = 0.60) (Fig. 3 (c)), less disruption to ripple structure can be seen when compared to DV7. However, the ripples in the vegetated area are smaller than those in the bare sediment bed area.

4.2. Hydrodynamics

This section analyses the hydrodynamics within the rigid vegetation arrays. Appendix A – Table A1 shows the percentage wave attenuation at the end of the vegetation meadow with respect to the wave height measured prior to the vegetation meadow for each test case [(H_s at WG4/H_s at WG1)%]. The dense vegetation, sparse vegetation, and bare sediment bed conditions led to 26%, 18% and 10% reductions in wave height respectively under the submerged vegetation conditions, and 31%, 18% and 10% reductions respectively under the emerged vegetation conditions. Compared with the bare sediment bed, dense vegetation provides the most significant wave attenuation, while sparse vegetation provides only slight wave height attenuation.

Understanding the impacts of vegetation on near-bed velocities can benefit our understanding of sediment transport through vegetation. Traditionally, $U_{w,bed}$ has been related to the initiation of sediment transport through methods such as those described in Section 2. It is widely acknowledged that as waves travel over vegetation, the work done against the stems attenuates wave height and velocity (Dalrymple et al., 1984; Lowe et al., 2005). Recent studies have also highlighted an increase in *TKE* through vegetation (Tinoco and Coco, 2014, 2018) and, therefore, a reduction in sediment suspension thresholds. Therefore, our analysis considered wave-induced velocity U_w, wave-induced velocity at the bed $U_{w,bed}$, and turbulent kinetic energy *TKE* in rigid vegetation to investigate the impact of vegetation stems on the hydrodynamics.

The near-bed area, defined as the area around 4 to 5 times of η_r above ripple crest (Thorne et al., 2003) is considered to be insignificantly influenced by the ripple-generated vortices. If *TKE* is measured at an elevation greater than this elevation above the bed, then the ripple-generated vortices may not be accounted for. Therefore, the *TKE* at the bed, (TKE_{bed}) values are taken at 1 cm above the bed (hereafter known as near-bed region) to ensure the maximum *TKE* values near the bed are captured. The $U_{w,bed}$ values (determined from measurements carried out by the PIV at the measurement window in Fig. 1) are also taken at 1 cm above the bed. The stem average *TKE* (TKE_{stem}) values are calculated by averaging the *TKE* values over the top 15 cm of the stem length (hereafter known as stem region). For reference, the *TKE* and velocity values on the bare sediment bed cases are also taken at the same locations. The results are presented relative to the bare sediment bed conditions. For example, the changes in the velocities in the stem region and near-bed region are given by $\Delta U_{w,stem} = \left(U_{w,stem,veg} - U_{w,stem,bare}\right)/U_{w,stem,bare}$ and $\Delta U_{w,bed} = \left(U_{w,bed,veg} - U_{w,bed,bare}\right)/U_{w,bed,bare}$, respectively in which $U_{w,stem,veg}$ is the U_w values within the vegetation averaged over the top 15 cm of the stem height and $U_{w,stem,bare}$ is the U_w values on bare sediment bed, averaged over the same region, similar to that determined on the vegetated bed. The same procedure is applied to the *TKE*. The results are presented in Fig. 4, which compares the values of $\Delta U_{w,stem}$, $\Delta U_{w,bed}$, ΔTKE_{stem}, and ΔTKE_{bed} between dense and sparse arrays.

According to Fig. 4(a) and (b), the dense vegetation led to greater attenuation of $\Delta U_{w,bed}$ and $\Delta U_{w,stem}$ than the sparse vegetation and bare sediment bed cases under the same wave conditions. This is valid for both emerged and submerged vegetation although emerged cases led to a more significant velocity attenuation than the submerged vegetation cases. These results demonstrate that the attenuation of velocity through the vegetation meadow shows the same trend as the wave height attenuation.

Fig. 4(c) presents the ΔTKE_{bed} versus A_w/S_x values. According to Fig. 4(c), generally, the existence of vegetation led to an insignificant reduction in the TKE_{bed} when compared to bare sediment bed although this effect is slightly stronger in the denser vegetation cases. No clear relationship was observed between ΔTKE_{bed} and A_w/S_x, and no significant difference is found between submerged and emerged cases from Fig. 4(c). In the stem region, stem-generated vortices should predominately govern the *TKE* production as the impact from ripples may be small. Following Ros et al. (2014), Fig. 4(d) shows stem-averaged ΔTKE_{stem}% against A_w/S_x. It can be seen that the existence of vegetation in general increases the intensity of *TKE* in the stem region compared to bare sediment bed (indicated by positive ΔTKE_{stem}%) for both submerged and emerged dense vegetation, and for emerged sparse vegetation. Mostly negative ΔTKE_{stem}% in submerged sparse vegetation cases indicate a reduction in *TKE* in the stem region of the water column when compared to that on a bare sediment bed. In dense vegetation, the increase of ΔTKE_{stem}% with the increase of A_w/S_x is clearly evident for $A_w/S_x > 0.5$. No clear relationship is found between ΔTKE_{stem}% and A_w/S_x when $A_w/S_x < 0.5$, although the negatives values for ΔTKE_{stem}% found in most cases indicates the fact that vegetation stems reduce the *TKE* in the stem region of the water column when compared to bare sediment beds.

In most cases, *TKE* in the stem region of the water column is larger than that on the bare sediment bed under the same wave conditions when $A_w/S_x > 0.5$, particularly for dense vegetation cases. Also, *TKE* is higher in emerged vegetation cases than in submerged vegetation. These observations align well with the experimental evidence of Zhang et al. (2018), who stated that the values of $A_w/S_x > 0.5$ led to an increase of *TKE* relative to bare sediment bed conditions. Similar results are also observed more recently by Tang et al. (2024). In sparse, emerged vegetation, ΔTKE_{stem}% values are positive and increase with A_w/S_x,when $A_w/S_x > 0.5$. In sparse, submerged vegetation, ΔTKE_{stem}% are mainly negative and no clear relashionship with A_w/S_x can be seen.

4.3. Near-bed sediment concentration

This section analyses the near-bed sediment concentration *C0*, on vegetated sediment beds. It should be noted that sediment

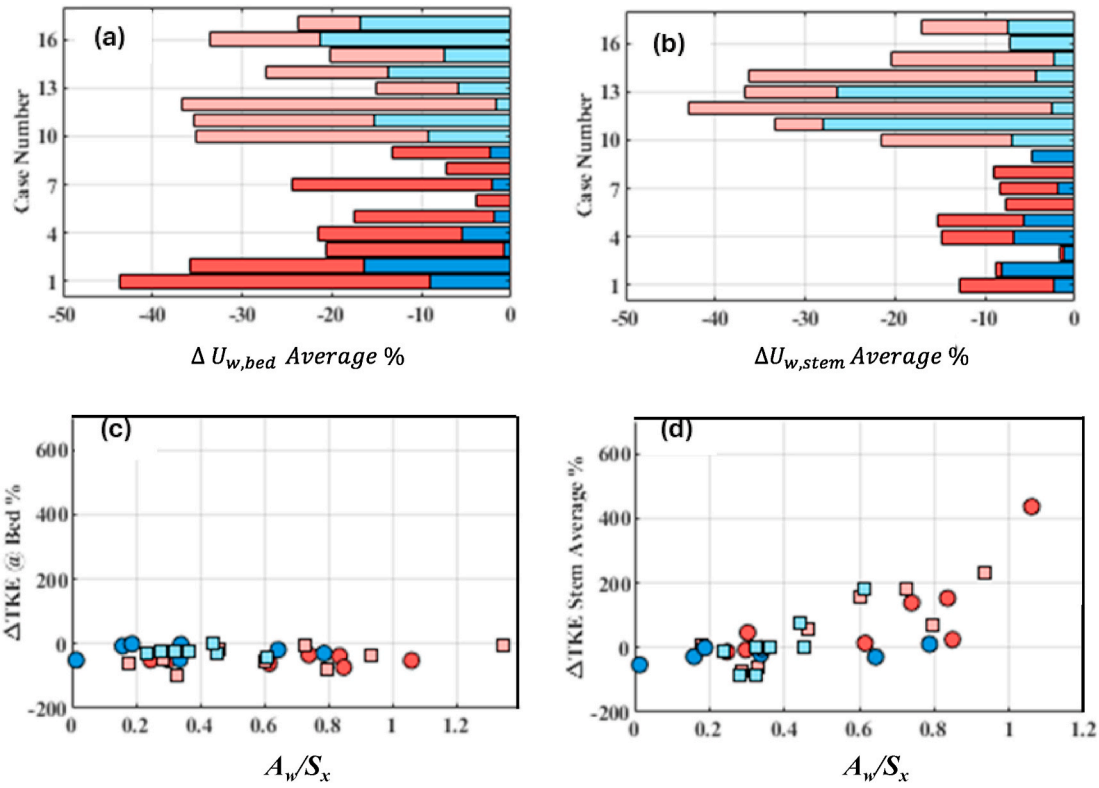

Fig. 4. (a) and (b) Averaged $\Delta U_{w,bed}$ and$\Delta U_{w,stem}$ percentages respectively for all test cases; (c) and (d) ΔTKE_{bed} and ΔTKE_{stem} percentage against A_w/S_x respectively. Cases 1 to 9 are submerged vegetation cases (circles), and 10 to 17 are emerged vegetation cases (squares). Blue represents sparse vegetation, and red represents dense vegetation. Lighter colours in refer to emerged vegetation while darker colours refer to emerged vegetation. (For interpretation of the references to colour in this figure legend, the reader is referred to the Web version of this article.)

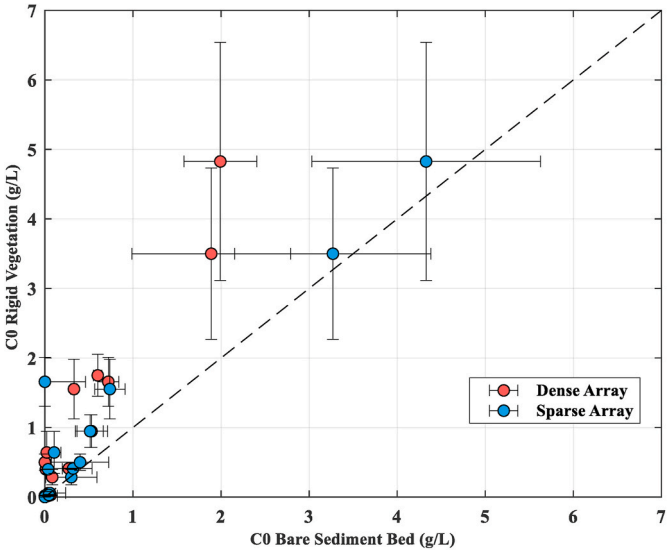

Fig. 5. The difference of near-bed sediment concentration C0 between vegetated and bare sediment bed under the same hydrodynamic conditions. Dashed line indicates bare sediment bed values under the same forcing conditions.

concentrations and hydrodynamics measured simultaneously at the measurement window shown in Fig. 1 are used in this analysis. In Fig. 5, *C0* in rigid vegetation cases are compared with those on bare sediment bed, under the same wave conditions. Only cases in which ripples have formed are considered in this section. For every dense vegetation case, a reduction in *C0* compared to bare sediment bed cases is observed, with a more significant reduction when *C0* is large. Sparse vegetation cases also

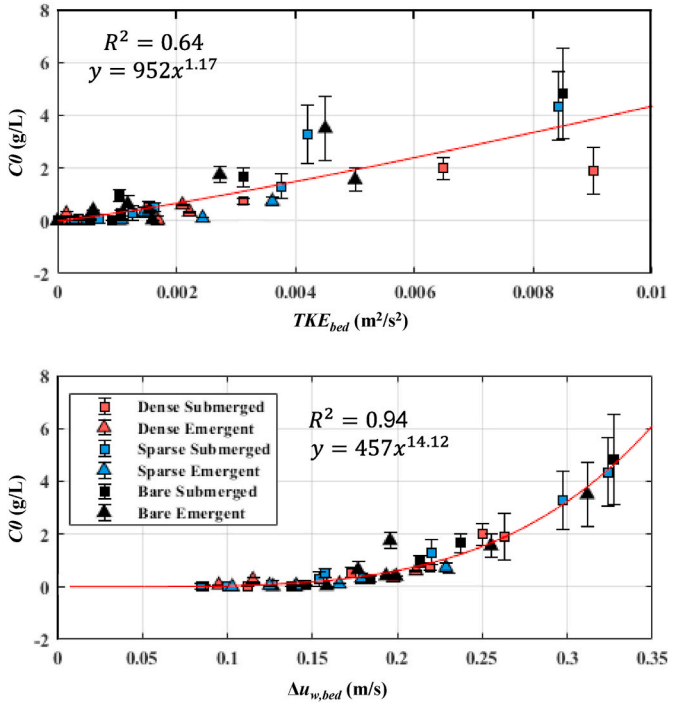

Fig. 6. Measured C0 plotted against near bed (a)TKE_{bed} and (b)$U_{w,bed}$, for all cases in Appendix A- Table 1. Error bands show the maximum variation in C0 either between the selected Z_{ref} value and the previous Z_{ref} bin, or between repeat experiments.

show a reduction in *C0* compared to bare sediment bed cases, only with a few exceptions. This is a result of the reduction in η_r and ripple steepness, which govern sediment suspension over rippled beds (Eq. (4)).

In the previous literature, *C0* has been related to $U_{w,bed}$ or *TKE* in the near-bed region (TKE_{bed}). Fig. 6 (a) and (b) show *C0* against TKE_{bed}, and $U_{w,bed}$, respectively. *TKE* fits an exponential relationship with *C0*, showing the goodness-of-fit, $R^2 = 0.64$. $U_{w,bed}$ also shows an exponential correlation with *C0*, with an $R^2 = 0.94$. It can be seen from Fig. 6 that the relationship of *C0* with TKE_{bed}, and $U_{w,bed}$ is similar, except for *C0* values greater than 3 g/L, irrespective of the stem density. This suggests the relationship between *C0* and TKE_{bed}, and $U_{w,bed}$ may be independent of stem density, at least for smaller values of *C0* (also seen in Fig. 4). Previous studies have shown that over flat, vegetated sediment beds without bed forms, *C0* increases with increasing stem array density for the same wave conditions (Tinoco and Coco, 2018; Lou et al., 2022; Tang et al., 2019), which is not observed on rippled sediment beds investigated in this study.

5. Discussion

5.1. The role of stem spacing and stem array density on ripple formation

Based on the experimental results presented in Section 4, it is evident that the presence of vegetation leads to wave attenuation, as observed by numerous previous studies and that generates turbulence around individual rigid stems, which is directly linked to altering the velocity field. This leads to the disruption of the ripples immediately around stems, especially in the case of dense vegetation. Sparse vegetation has either a less significant effect or no effect on ripples based on the incident wave conditions.

These observations partially agreed with the results of Zhang and Nepf (2019), while some discrepancies are found especially when $A_w/S_x > 0.5$. Zhang and Nepf (2019) suggested complete removal of ripples within vegetation meadows, especially when $A_w/S_x > 0.5$ while our study found a significant disruption to the ripple structure in dense vegetation, instead of being entirely washed out. When $A_w/S_x > 0.5$, stem-generated vortices can remove sediment from the area immediately upstream or downstream of the stems, however, A_w/S_x alone may not be a sufficient parameter to define ripple formation within rigid arrays.

5.2. TKE generated by stems and ripples

Here we use the 'wave fraction (*WF*) proposed by Nepf et al. (1997) to investigate ripples on vegetated beds. *WF* is taken as the area fraction occupied by a turbulent wake per square meter of the bed area, which is calculated as the product of vegetation stem density (N_v) and the area of a turbulent wake generated by a single stem per square meter of the bed (*M*). *M* has been shown to vary between 10 within an array of cylinders to 40 for a single stem (Nepf et al., 1997; Zavistoski, 1994). Adopting the findings of Zavistoski (1994) where the width of a wake is taken as $2b_v$ and the findings of Zhang et al. (2018) where the stem-generated wakes were observed to travel A_w both upstream and downstream side of the stem in the wave propagation direction, $M = 2A_w 2b_v$. Therefore, $WF = M \times N_v$. A conceptual diagram illustrating the impact of stem array density on *WF* and corresponding ripple formation is provided in Fig. 7.

To explore the relationship between *WF* and ripple formation, the *WF* values were calculated based on the dataset from Table A1 of Appendix A and the dataset from Zhang and Nepf (2019). By interrogating the results obtained by the bed profiler on ripple formation on the vegetated sediment bed, we found that ripples do not form when $WF > 60\%$. Thus, we propose a criterion to identify the condition to be satisfied for a total washing out of ripples on rigid vegetation as: (i) $A_w/S_x > 0.5$, and (ii) $WF > 60\%$.

The proposed criteria are tested in Fig. 8, which shows a plot of *WF* *vs.* A_w/S_x based on both our experimental data (black squares) and the dataset from Zhang and Nepf (2019) (green squares). It can be seen that the criteria proposed by the present study ($A_w/S_x > 0.5$ and $WF > 60\%$), shown in dark black horizontal and vertical lines, divided the results into four zones: Zones 1 and 2 stand for the cases in which the stem-generated vortices remain very close to the stem, in the sparse and dense vegetation cases respectively. The majority of the cases in the present study, while fell into Zone 1, which showed well-shaped ripples. None of our data fell into Zone 2. Zone 3 includes cases with higher stem densities where turbulent wakes impact the entire bed due to closely packed stems. As a result, no ripple formation is observed from the cases in Zone 3, as observed by Zhang and Nepf (2019). Zone 4 includes sparse vegetation cases with turbulent wakes extending between stems in the

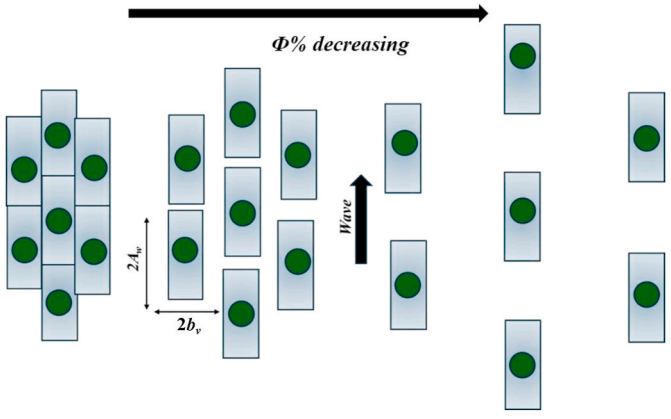

Fig. 7. Conceptual sketch of TKE distribution in rigid vegetation in a staggered vegetation stem array. Blue rectangles represent the area of stem-generated TKE, and green circles represent vegetation. (For interpretation of the references to colour in this figure legend, the reader is referred to the Web version of this article.)

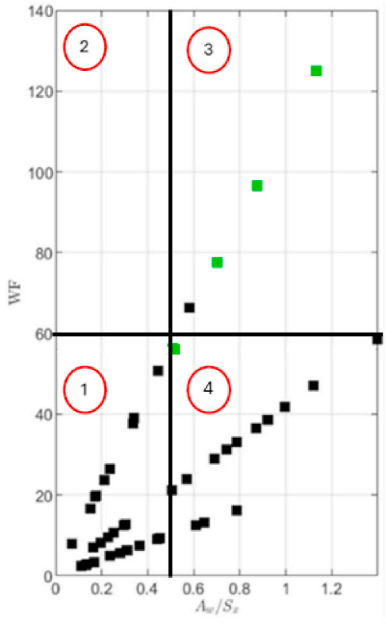

Fig. 8. A plot of A_w/S_x versus WF, using the rigid vegetation dataset from the present study (black squares) and a part of Zhang and Nepf (2019) dataset where ripples are washed out and formed a flat sediment bed (green squares). The criteria proposed by the present study ($A_w/S_x = 0.5$ and $WF = 60\%$) divide the plot into zones 1, 2, 3, and 4. (For interpretation of the references to colour in this figure legend, the reader is referred to the Web version of this article.)

direction of wave propagation. Although still intact, a significant ripple disruption is observed in this region. Based on these findings, it is clear that the ripple deformation can be linked with stem density and the area coverage of stem-generated turbulence. However, further studies focusing on a wide range of array densities and configurations are required to consolidate this finding.

Both TKE_{stem} and TKE_{bed} characterises the flow structure within a vegetation meadow. Previous studies where either a vegetated flat sediment bed was used (Tinoco and Coco, 2018; Zhang et al., 2018; Tang et al., 2019; Lou et al., 2022) or the bed did not include sediment (Zhang et al., 2018; Tang et al., 2024) have shown that TKE_{stem} and TKE_{bed} are higher within vegetation canopies compared to that on bare sediment beds, despite the reduction of velocity by vegetation. Our results, which included rippled sediment beds, show that while the presence of vegetations significantly increases the TKE_{stem} (Fig. 6(d)), TKE_{bed} in cases with and without vegetation does not differ significantly, irrespective of the vegetation density (Fig. 6(c)). This confirms that although vegetation stems are present, ripples dominate the near-bed *TKE* generation, similar to that found in bare sediment bed cases (Nielsen, 1986; Thorne et al., 2002, 2009). However, it should be noted that the vegetation can attenuate the near-bed velocity, alter the ripple structure, and influence ripple dimensions thus indirectly impacting seabed dynamics and sediment suspension.

5.3. Suspended sediment concentration

Suspended sediment concentration is a key parameter that determines bed erosion and instability. As discussed in the previous sections, the ripples can form within sparse and dense vegetation meadows, and the vegetation influences *C0* by attenuating the velocity and changing the ripple structure. The *C0* values on rippled beds are dominated by the ripples. Previous studies have found that the ripple steepness governs the suspension of sediment (e.g. Davies and Villaret,1999; Thorne et al., 2002).

While methods have been proposed to predict the *C0* over bare sediment beds without vegetation (Nielsen, 1986; see Section 2), a method to predict the *C0* over vegetated rippled beds is not available. However, due to the dominant role of the ripples on *C0*, coupled with the reduction of $U_{w,bed}$ at the bed due to disrupted ripples among vegetation, it is reasonable to hypothesise that existing methods that incorporate $U_{w,bed}$ for predicting *C0* over bare sediment bed rippled beds could still be applied to determine the *C0* on vegetated beds.

Based on this hypothesis, we adopted the equations of Nielsen (1986) (Eqs. (1)–(4)), to estimate the ripple dimensions, as well as the *C0* on vegetated sediment bed cases in the present study. Firstly, *C0* values on the bare sediment bed were used to determine the coefficient γ in the equations. It was found that $\gamma = 0.0048$, which is comparable to the value provided by Nielsen (1986), i.e. $\gamma = 0.005$. $\gamma = 0.0048$ was then used to predict *C0* values for dense and sparse vegetation cases under different hydrodynamic conditions using Eq. (3). Fig. 9 compares the measured *C0* with the values predicted by Nielsen (1986). The goodness of fit between predicted and actual are provided through R^2 and normalised root mean squared error (NRMSE) were also calculated, as shown in Fig. 9. For all three conditions, involving bare sediment bed, dense vegetation, and sparse vegetation cases, the R^2 values are above 0.82 and the NRMSE between measured and predicted values varies between 0.057 and 0.107. This suggests a good agreement between the measured *C0* values and the values predicted using Nielsen's (1986). This result confirms that Nielsen's (1986) formulation can be used to determine *C0* on vegetated sandy sea beds as a first approximation although further work is needed to extend its validity over a wide range of conditions.

6. Conclusion

A series of laboratory experiments were conducted in a wave flume to investigate the impacts of rigid vegetation on suspended sediment concentration and ripple formation on a sandy bed. The experiments involve a range of wave conditions, two vegetation densities, and both submerged and emerged vegetation meadows. The same experiments were repeated on a bare sediment bed, which were taken as the baseline.

Wave attenuation was observed over the length of the vegetation meadow. The intensity of wave attenuation varied with vegetation density and depended on wave conditions. U_w was also reduced as a result. Dense vegetation led to a more significant wave attenuation. In the stem region (from the bed up to the top of the stems), under the same wave conditions, the vegetated cases show larger *TKE* values than the bare sediment bed cases when $A_w/S_x > 0.5$. At the bed, *TKE* values on vegetated beds were comparable to those on the bare sediment bed. This shows that the ripple-generated *TKE* dominates the near-bed *TKE*.

Ripple formation was observed on both bare sediment beds and vegetated beds, while the presence of vegetation alters the ripple

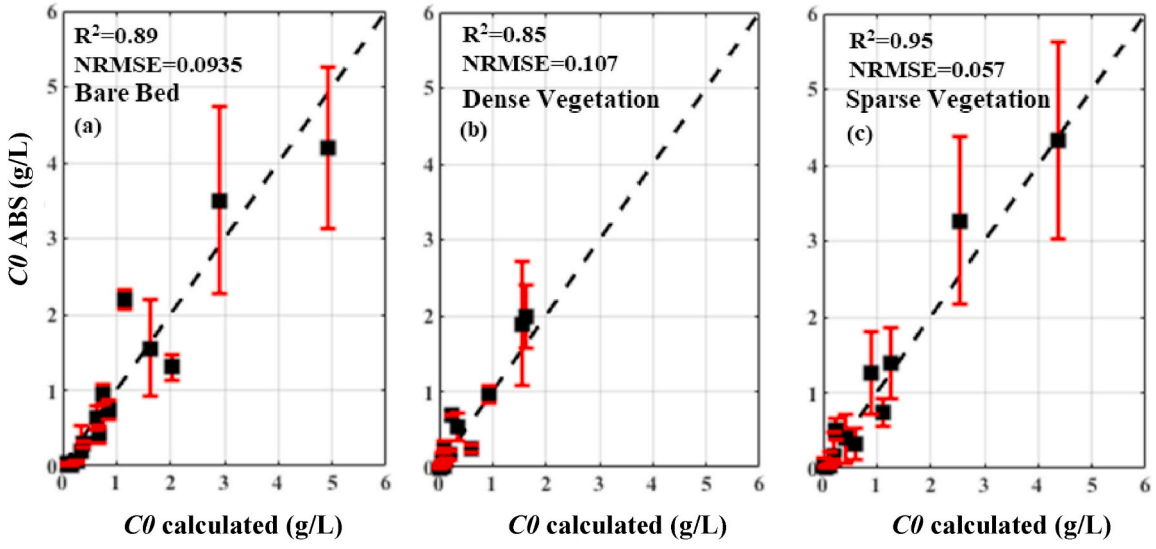

Fig. 9. Calculated values of C0 using Eq. (3) vs measured values of C0, with error bands being the variation in C0 between the selected Z_{ref} value and the previous Z_{ref} vertical bin. Dashed black line indicates the 1:1 fit.

structure and dimensions. When $A_w/S_x > 0.5$, ripple formation in the stem-wake region was significantly obstructed by the stems. The stem density plays a crucial role in disrupting ripples. Ripple formation is less hindered within sparse vegetation. This can be quantified through an adapted Wake Fraction parameter, where ripples were found to be disrupted when $WF > 60\%$. Therefore, the criteria to be satisfied for total washout of the ripples is proposed to be $A_w/S_x > 0.5$ and $WF > 60\%$.

Both sparse and dense vegetation reduce the sediment suspension and *C0* compared to bare sediment beds, under the same wave conditions. The origins of this reduction are two folds: (i) the near-bed orbital velocity is attenuated due to the vegetation; and (ii) the significant deformation of the ripples weakens the *TKE* on rippled beds which governs sediment suspension. In the near-bed region, ripples dominate the generation of *TKE*.

The near-bed sediment concentration was dependent on vegetation density and $U_{w,bed}$. A higher stem array density leads to a higher reduction of *C0*. When the criteria we proposed ($A_w/S_x > 0.5$ and $WF > 60\%$) are exceeded, the ripples will be partially or fully washed out (and *C0* will be significantly reduced, as shown in Fig. 8(a)). It should be noted that it is still challenging to accurately quantify the influence of vegetation on the values of *C0*. However, by applying the formulae proposed by Nielsen (1986) on the experimental data of the present study, we demonstrated the applicability of the conventional method applied to bare sediment beds to rippled and vegetated sandy beds, for the prediction of the near-bed reference sediment concentration. Further investigation converting a wide range of experimental conditions is needed to extend the validity of this method.

The findings of this study contribute to enabling more accurate predictions of suspended sediment concentration over vegetated sandy beds. In the context of restoration, it is highlighted that vegetation can encourage sediment retention and erosion reduction compared to regions without vegetation. By reducing the sediment concentration, the light penetration in the water column can be improved under certain conditions. These benefits emphasise their potential use as nature-based solutions. However, it should be noted that further investigations covering a wide variety of vegetation densities and plant rigidities are required to generalise our findings. First, future studies should pay particular attention to stem configuration and varying densities to fully capture the stem-stem interactions and their impact on sediment mobility. Second, the role of plant rigidity needs to be explored to capture stem-wake impacts from semi-rigid or fully flexible vegetation and the resultant impact on sediment erosion.

CRediT authorship contribution statement

K. Ions: Writing – review & editing, Writing – original draft, Methodology, Investigation, Formal analysis, Data curation, Conceptualization. **X. Wang:** Investigation, Writing – review & editing. **D.E. Reeve:** Writing – review & editing, Supervision, Methodology, Conceptualization. **N. Mori:** Writing – review & editing, Supervision, Funding acquisition. **H. Karunarathna:** Writing – review & editing, Validation, Supervision, Project administration, Methodology, Funding acquisition, Conceptualization.

Plain language summary

Coastal vegetation can mitigate floods and coastal erosion. The key physical processes that underpin sediment suspension through vegetation under waves over rippled sandy beds are studied using a series of laboratory experiments. The impact vegetation has on ripple formation and the subsequent sediment suspension is unravelled, revealing denser vegetation can reduce sediment suspension.

Open research

Data archiving is underway, using the repository 'Figshare' – the private DOI for reviewers use only is https://figshare.com/s/511ecd5aebb7a41e0416.

Declaration of Competing Interest

The authors declare the following financial interests/personal relationships which may be considered as potential competing interests: Kristian Ions reports financial support was provided by Engineering and Physical Sciences Research Council. If there are other authors, they declare that they have no known competing financial interests or personal relationships that could have appeared to influence the work reported in this paper.

Acknowledgments

This research is supported by the Engineering and Physical Sciences Research Council (EPSRC) UK Doctoral Training Partnership of Swansea University (EP/T517987/1) grant. We would like to thank Dr. J.M. Horrillo-Caraballo for the assistance during the experiments. HK and XW acknowledges Leverhulme Trust Research Grant RPG-2023-235. We also extend thanks to The Great British Sasakawa Foundation grant No. 6365 and the Disaster Prevention Research Institute (DPRI) of Kyoto University International Collaborative Research Grant 2023IG-02 for facilitating research collaboration between Swansea University and DPRI. NM is also supported by JICA/JST SATREPS Program (JPMJSA2110).

Appendix A

Appendix A - Table A1
List of experimental conditions in this study. Subscript a indicates measured values and subscript b indicates calculated values using Eqs. (1) and (2).

CASE	*Hs (m)*	*T (s)*	*kh*	U_{bed}*(m/s)*	h_v/h	*Nv*	φ	A_w *(cm)*	A_w/S_x	*RE*	*KC*	η_r (cm)*a, b*	λ_r(cm)*a, b*	η_r/λ_r	H_s at WG4/H_s (%)
B1	0.1	1	1.89	0.11	0.66	0	0	1.79	inf	562	22.48	0.00[a]	0.00[a]	0	91.1
B2	0.12	1	1.89	0.13	0.66	0	0	2.06	inf	647.5	25.9	0.00[a]	0.00[a]	0	91
B3	0.15	1	1.89	0.14	0.66	0	0	2.21	inf	694	27.76	0.55[a]	0.00[a]	0.19	87
B4	0.1	1.5	1.04	0.18	0.66	0	0	4.25	inf	890	53.4	0.79[a]	4.02[a]	0.2	90.9
B5	0.12	1.5	1.04	0.21	0.66	0	0	4.91	inf	1 028.5	61.71	1.05[a]	6.13[a]	0.17	93.7
B6	0.15	1.5	1.04	0.23	0.66	0	0	5.43	inf	1 137.5	68.25	0.93[a]	6.03[a]	0.15	94.6
B7	0.2	1.5	1.04	0.33	0.66	0	0	7.9	inf	1 654	99.24	1.19[a]	7.42[a]	0.16	94.5
B8	0.1	2	0.73	0.19	0.66	0	0	5.95	inf	934	74.72	1.16[a]	5.98[a]	0.19	91.1
B9	0.15	2	0.73	0.3	0.66	0	0	9.63	inf	1 513	121.04	1.15[a]	7.67[a]	0.15	93.1
B10	0.06	1	1.89	0.11	1	0	0	1.76	inf	554	22.16	0.00[a]	0 .00[a]	0	89.3
B11	0.08	1	1.89	0.15	1	0	0	2.34	inf	735.5	29.42	0.54[a]	3.06[a]	0.17	97.5

(*continued on next page*)

Appendix A - Table A1 (*continued*)

CASE	*Hs (m)*	*T (s)*	*kh*	U_{bed}*(m/s)*	h_v/h	*Nv*	*φ*	A_w *(cm)*	A_w/S_x	*RE*	*KC*	η_r (cm)*a, b*	λ_r(cm)*a, b*	η_r/λ_r	H_s at WG4/H_s (%)
B12	0.1	1	1.89	0.18	1	0	0	2.8	inf	880.5	35.22	0.59[a]	3.19[a]	0.19	90.3
B13	0.06	1.5	1.04	0.15	1	0	0	3.46	inf	724.5	43.47	0.75[a]	4.39[a]	0.17	97.7
B14	0.08	1.5	1.04	0.21	1	0	0	4.55	inf	952	57.12	0.99[a]	5.33[a]	0.19	93
B15	0.1	1.5	1.04	0.25	1	0	0	5.8	inf	1 214	72.84	0.91[a]	6.02[a]	0.15	98.2
B16	0.06	2	0.73	0.21	1	0	0	5.45	inf	855.5	68.44	1.19[a]	6.23[a]	0.19	96.3
B17	0.08	2	0.73	0.28	1	0	0	6.76	inf	1 061.5	84.92	1.36[a]	7.28	0.19	96.0
DV1	0.1	1	1.89	0.06	0.66	342	0.67	1.48	0.25	465.53	18.62	0.00[b]	0.00[b]	0	81.5
DV2	0.12	1	1.89	0.09	0.66	342	0.67	1.94	0.32	608.16	24.33	0.00[b]	0.00[b]	0	82.6
DV3	0.15	1	1.89	0.11	0.66	342	0.67	2.38	0.4	748.93	29.96	0.27[b]	1.78[b]	0.15	74.2
DV4	0.1	1.5	1.04	0.14	0.66	342	0.67	3.7	0.62	773.93	46.44	0.51[b]	3.40[b]	0.15	82.6
DV5	0.12	1.5	1.04	0.17	0.66	342	0.67	4.44	0.74	930.25	55.81	0.61[b]	4.09[b]	0.15	85.9
DV6	0.15	1.5	1.04	0.22	0.66	342	0.67	5.16	0.86	1 081.3	64.88	0.77[b]	5.14[b]	0.15	83.4
DV7	0.2	1.5	1.04	0.25	0.66	342	0.67	5.63	0.94	1 179.89	70.79	0.88[b]	5.84[b]	0.15	79.0
DV8	0.1	2	0.73	0.17	0.66	342	0.67	5.73	0.95	900	72	0.81[b]	5.41[b]	0.15	82.5
DV9	0.15	2	0.73	0.26	0.66	342	0.67	8.09	1.35	1 271.2	101.7	1.21[b]	8.04[b]	0.15	84.8
DV10	0.06	1	1.89	0.07	1	342	0.67	1.09	0.18	341.14	13.65	0.00[b]	0.00[b]	0	76.6
DV11	0.08	1	1.89	0.09	1	342	0.67	1.71	0.29	537.4	21.5	0.23[b]	1.51[b]	0	73.1
DV12	0.1	1	1.89	0.12	1	342	0.67	1.53	0.25	479.33	19.17	0.27[b]	1.83[b]	0.15	72.3
DV13	0.06	1.5	1.04	0.13	1	342	0.67	2.77	0.46	579.27	34.76	0.00[b]	0.00[b]	0	79
DV14	0.08	1.5	1.04	0.15	1	342	0.67	3.62	0.6	757.14	45.43	0.55[b]	3.65[b]	0.15	76.9
DV15	0.1	1.5	1.04	0.2	1	342	0.67	4.78	0.8	1 000.74	60.04	0.70[b]	4.65[b]	0.15	75.7
DV16	0.06	2	0.73	0.14	1	342	0.67	5.6	0.93	879	70.32	0.61[b]	4.09[b]	0.15	83
DV17	0.08	2	0.73	0.21	1	342	0.67	6.46	1.08	1 015.48	81.24	0.98[b]	6.54[b]	0.15	88.3
SV1	0.1	1	1.89	0.1	0.66	80	0.16	1.83	0.15	574.5	22.98	0.00[a]	0.00[a]	0	84.2
SV2	0.12	1	1.89	0.12	0.66	80	0.16	2.08	0.17	655	26.2	0.00[a]	0.00[a]	0.21	86.8
SV3	0.15	1	1.89	0.18	0.66	80	0.16	2.88	0.24	904.5	36.18	0.86[a]	3.92[a]	0.22	81.8
SV4	0.1	1.5	1.04	0.14	0.66	80	0.16	3.36	0.28	703	42.18	0.73[a]	5.01[a]	0.15	89.2
SV5	0.12	1.5	1.04	0.18	0.66	80	0.16	4.36	0.36	914	54.84	1.22	5.89[a]	0.21	90.4
SV6	0.15	1.5	1.04	0.23	0.66	80	0.16	5.46	0.45	1 142.5	68.55	1.59[a]	6.51[a]	0.18	91.1
SV7	0.2	1.5	1.04	0.17	0.66	80	0.16	3.96	0.33	829	49.74	1.18[a]	6.05[a]	0.2	90
SV8	0.1	2	0.73	0.23	0.66	80	0.16	7.33	0.61	1 151.5	92.12	1.55[a]	7.00[a]	0.22	90.6
SV9	0.15	2	0.73	0.08	0.66	80	0.16	3.21	0.27	505	40.4	1.43[a]	7.23[a]	0.2	90.7
SV10	0.06	1	1.89	0.1	1	80	0.16	1.91	0.16	599.5	23.98	0.48[a]	2.56[a]	0.19	84.3
SV11	0.08	1	1.89	0.13	1	80	0.16	2.32	0.19	728.5	29.14	0.62[a]	3.24[a]	0.19	83.5
SV12	0.1	1	1.89	0.15	1	80	0.16	2.7	0.22	847.5	33.9	1.32[a]	5.52[a]	0.2	82.7
SV13	0.06	1.5	1.04	0.16	1	80	0.16	4.09	0.34	856	51.36	1.33[a]	6.34[a]	0.21	88.6
SV14	0.08	1.5	1.04	0.25	1	80	0.16	5.94	0.49	1 243.5	74.61	1.53[a]	7.69[a]	0.2	91.9
SV15	0.1	1.5	1.04	0.32	1	80	0.16	7.73	0.64	1 618	97.08	1.43[a]	8.64[a]	0.17	87.7
SV16	0.06	2	–	–	1	80	0.16	–	–	–	–	–	–	–	–
SV17	0.08	2	0.73	0.3	1	80	0.16	9.45	0.79	1 484.5	118.76	1.69[a]	8.58[a]	0.2	88.4

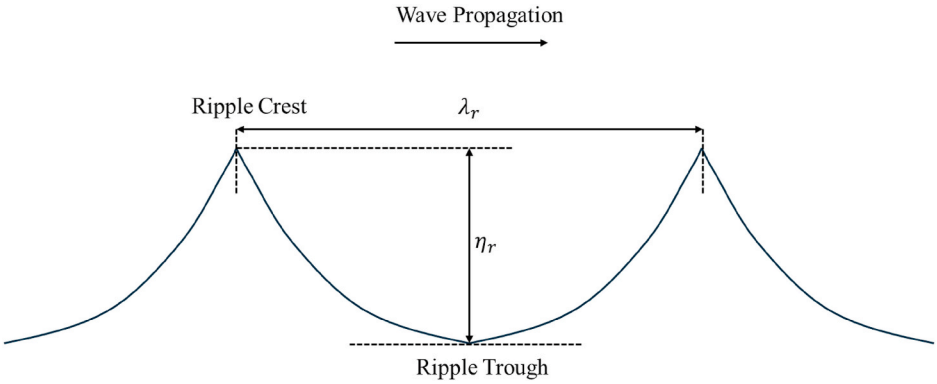

Appendix A - Fig. A1. Example sketch of typical ripple formation, where λ_r is ripple wavelength, defined as the distance between ripple crests and η_r is ripple crest height, defined at the distance from trough to crest.

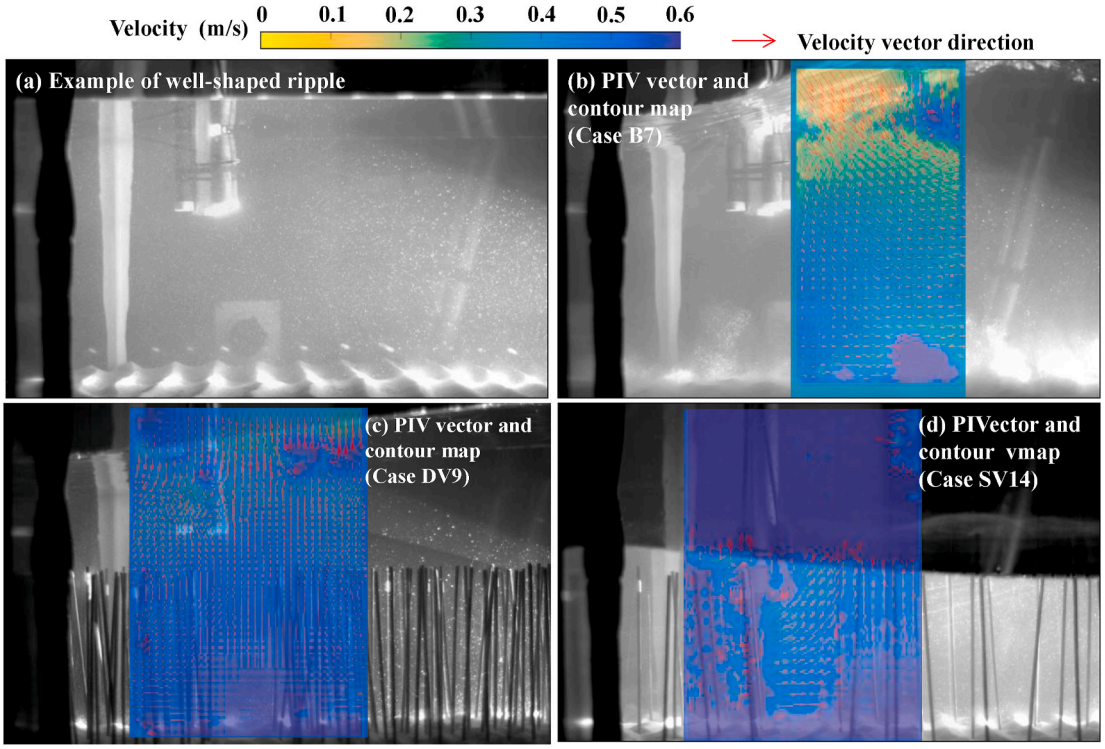

Appendix A Fig. A2(a). Example of well-shaped ripples captured by the high-speed camera; (b), (c) and (d) are examples of the PIV vector map and magnitude contour plot for cases B7, DV9 and SV14, respectively.

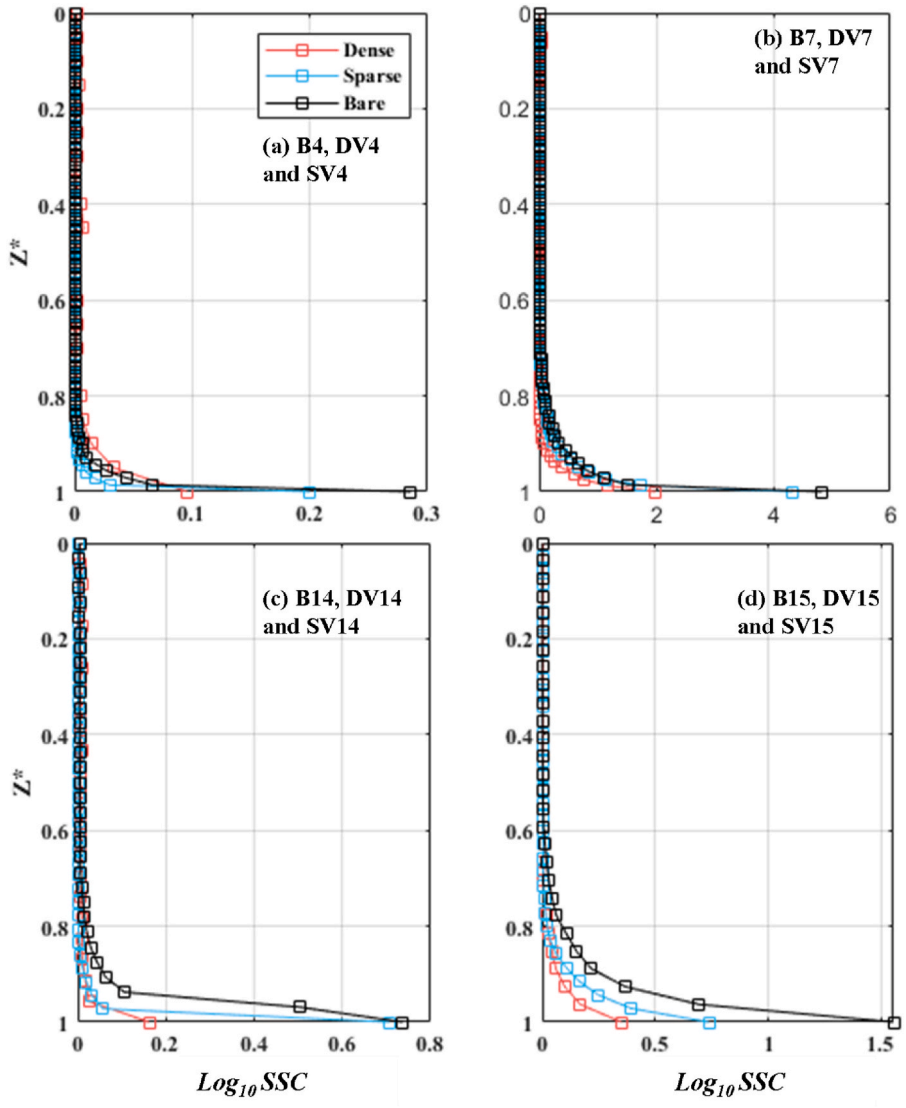

Appendix A - Fig. A3. Example cases of the mean SSC profiles recorded using ABS. Z* is the normalised water depth.

Data availability

Data will be made available on request.

References

Anderson, M.E., Smith, J.M., 2014. Wave attenuation by flexible, idealised salt marsh vegetation. Coast. Eng. 83, 82–92. https://doi.org/10.1016/j.coastaleng.2013.10.004.

Barbier, E.B., Hacker, S.D., Kennedy, C., Koch, E.W., Stier, A.C., Silliman, B.R., 2011. The value of estuarine and coastal ecosystem services. Ecol. Monogr. 81 (2), 169–193. https://doi.org/10.1890/10-1510.1.

Bennett, W.G., van Veelen, T.J., Fairchild, T.P., Griffin, J.N., Karunarathna, H., 2020. Computational modelling of the impacts of saltmarsh management interventions on hydrodynamics of a small macro-tidal estuary. J. Mar. Sci. Eng. 8 (5), 373. https://doi.org/10.3390/jmse8050373.

Bouma, T.J., Vries, M.D., Low, E., Kusters, L., Herman, P.M.J., Tanczos, I.C., Temmerman, S., Hesselink, A., Meire, P., Regenmortel, S.V., 2005. Flow hydrodynamics on a mudflat and in salt marsh vegetation: identifying general relationships for habitat characterisations. Hydrobiologia 540, 259–274.

Brevik, I., Bjørn, A., 1979. Flume experiment on waves and currents. I. Rippled bed. Coast. Eng. 3, 149–177. https://doi.org/10.1016/0378-3839(79)90019-X.

Chen, Y., Li, Y., Thompson, C., Wang, X., Cai, T., Chang, Y., 2018. Differential sediment trapping abilities of mangrove and saltmarsh vegetation in a subtropical estuary. Geomorphology 318, 270–282. https://doi.org/10.1016/j.geomorph.2018.06.018.

Clifton, H.E., 1976. Wave-formed Sedimentary Structures—A Conceptual Model. https://doi.org/10.2110/pec.76.24.0126.

Dalrymple, R.A., Kirby, J.T., Hwang, P.A., 1984. Wave diffraction due to areas of energy dissipation. J. Waterw. Port, Coast. Ocean Eng. 110 (1), 67–79.

Davies, A.G., Villaret, C., 1999. Eulerian drift induced by progressive waves above rippled and very rough beds. J. Geophys. Res.: Oceans 104 (C1), 1465–1488. https://doi.org/10.1029/1998JC900016.

Davies, A.G., Villaret, C., 2002. Prediction of sand transport rates by waves and currents in the coastal zone. Cont. Shelf Res. 22 (18–19), 2725–2737. https://doi.org/10.1016/s0278-4343(02)00123-1.

Du Toit, C.K., Sleath, J.F.A., 1981. Velocity measurements close to rippled beds in oscillatory flow. J. Fluid Mech. 112, 71–96. https://doi.org/10.1017/s002211208100030x.

Fagherazzi, S., Bryan, K.R., Nardin, W., 2017. Buried alive or washed away: the challenging life of mangroves in the Mekong Delta. Oceanography (Wash., D.C.) 30 (3), 48–59. https://doi.org/10.5670/oceanog.2017.313.

Fagherazzi, S., Mariotti, G., Leonardi, N., Canestrelli, A., Nardin, W., Kearney, W.S., 2020. Salt marsh dynamics in a period of accelerated sea level rise. J. Geophys. Res.: Earth Surf. 125 (8), e2019JF005200. https://doi.org/10.1029/2019JF005200.

Fairchild, T.P., Bennett, W.G., Smith, G., Day, B., Skov, M.W., Möller, I., Beaumont, N., Karunarathna, H., Griffin, J.N., 2021. Coastal wetlands mitigate storm flooding and associated costs in estuaries. Environ. Res. Lett. 16 (7), 074034.

Fourqurean, J.W., Duarte, C.M., Kennedy, H., Marbà, N., Holmer, M., Mateo, M.A., et al., 2012. Seagrass ecosystems as a globally significant carbon stock. Nat. Geosci. 5 (7), 505–509. https://doi.org/10.1038/ngeo1477.

Fredsøe, J., Deigaard, R., 1992. Mechanics of coastal sediment transport, Vol. 3. World Scientific Publishing Company.

Furukawa, K., Wolanski, E., Mueller, H., 1997. Currents and sediment transport in mangrove forests. Estuar. Coast Shelf Sci. 44 (3), 301–310. https://doi.org/10.1006/ecss.1996.0120.
Gambi, M.C., Nowell, A.R., Jumars, P.A., 1990. Flume observations on flow dynamics in Zostera marina (eelgrass) beds. Mar. Ecol. Prog. Ser. 159–169.
Ghisalberti, M., Nepf, H.M., 2002. Mixing layers and coherent structures in vegetated aquatic flows. J. Geophys. Res.: Oceans 107 (C2), 1–3. https://doi.org/10.1029/2001JC000871.
Ghisalberti, M., Schlosser, T., 2013. Vortex generation in oscillatory canopy flow. J. Geophys. Res.: Oceans 118 (3), 1534–1542. https://doi.org/10.1002/jgrc.20073.
Gillis, L.G., Maza, M., Garcia-Maribona, J., Lara, J.L., Suzuki, T., Cierco, M.A., et al., 2022. Living on the edge: how traits of ecosystem engineers drive bio-physical interactions at coastal wetland edges. Adv. Water Resour. 166, 104257.
Giri, C., Ochieng, E., Tieszen, L.L., Zhu, Z., Singh, A., Loveland, T., et al., 2011. Status and distribution of mangrove forests of the world using earth observation satellite data. Global Ecol. Biogeogr. 20 (1), 154–159. https://doi.org/10.1111/j.1466-8238.2010.00584.x.
Goldstein, E.B., Coco, G., Murray, A.B., 2013. Prediction of wave ripple characteristics using genetic programming. Cont. Shelf Res. 71, 1–15. https://doi.org/10.1016/j.csr.2013.09.020.
Government, UK, 2021. Chief Medical Officer's annual report 2021: health in coastal communities. https://www.gov.uk/government/publications/chief-medical-officers-annual-report-2021-health-in-coastal-communities.
Gracia, A.D., Rangel-Buitrago, N., Oakley, J.A., Williams, A.T., 2018. Use of ecosystems in coastal erosion management. Ocean Coast Manag. 156, 277–289. https://doi.org/10.1016/j.ocecoaman.2017.07.009.
Green, M.O., Black, K.P., 1999. Suspended-sediment reference concentration under waves: field observations and critical analysis of two predictive models. Coast. Eng. 38 (3), 115–141. https://doi.org/10.1016/S0378-3839(99)00044-7.
Green, M.O., Coco, G., 2014. Review of wave-driven sediment resuspension and transport in estuaries. Rev. Geophys. 52 (1), 77–117. https://doi.org/10.1002/2013RG000437.
Green, E.P., Short, F.T., 2003. Centre mondial de surveillance continue de la conservation de la nature, & Programme des Nations Unies pour l'environnement, Vol. 298. World atlas of seagrasses, Berkeley.
Hansen, J.C., Reidenbach, M.A., 2012. Wave and tidally driven flows in eelgrass beds and their effect on sediment suspension. Mar. Ecol. Prog. Ser. 448, 271–287. https://doi.org/10.3354/meps09225.
Hansen, J.C., Reidenbach, M.A., 2013. Seasonal growth and senescence of a Zostera marina seagrass meadow alters wave-dominated flow and sediment suspension within a coastal bay. Estuaries Coasts 36, 1099–1114. https://doi.org/10.1007/s12237-013-9620-5.
Himes-Cornell, A., Pendleton, L., Atiyah, P., 2018. Valuing ecosystem services from blue forests: a systematic review of the valuation of salt marshes, sea grass beds and mangrove forests. Ecosyst. Serv. 30, 36–48. https://doi.org/10.1016/j.ecoser.2018.01.006.
Horppila, J., Nurminen, L., 2003. Effects of submerged macrophytes on sediment resuspension and internal phosphorus loading in Lake Hiidenvesi (southern Finland). Water Res. 37 (18), 4468–4474. https://doi.org/10.1016/S0043-1354(03)00405-6.
Horstman, E.M., Dohmen-Janssen, C.M., Narra, P.M.F., Van den Berg, N.J.F., Siemerink, M., Hulscher, S.J., 2014. Wave attenuation in mangroves: a quantitative approach to field observations. Coast. Eng. 94, 47–62. https://doi.org/10.1016/j.coastaleng.2014.08.001.
Hu, Z., Suzuki, T., Zitman, T., Uittewaal, W., Stive, M., 2014. Laboratory study on wave dissipation by vegetation in combined current–wave flow. Coast. Eng. 88, 131–142. https://doi.org/10.1016/j.coastaleng.2014.02.009.
Hugo, G., 2011. Future demographic change and its interactions with migration and climate change. Glob. Environ. Change 21, S21–S33. https://doi.org/10.1016/j.gloenvcha.2011.09.008.
Infantes, E., Orfila, A., Simarro, G., Terrados, J., Luhar, M., Nepf, H., 2012. Effect of a seagrass (Posidonia oceanica) meadow on wave propagation. Mar. Ecol. Prog. Series 456, 63–72.
Inman, D.L., 1957. Wave-generated ripples in nearshore sands (No. 100). US Beach Erosion Board.
Jadhav, R.S., Chen, Q., Smith, J.M., 2013. Spectral distribution of wave energy dissipation by salt marsh vegetation. Coast. Eng. 77, 99–107. https://doi.org/10.1016/j.coastaleng.2013.02.013.
Kathiresan, K., 2003. How do mangrove forests induce sedimentation? Rev. Biol. Trop. 51 (2), 355–360.
Kirezci, E., Young, I.R., Ranasinghe, R., Muis, S., Nicholls, R.J., Lincke, D., Hinkel, J., 2020. Projections of global-scale extreme sea levels and resulting episodic coastal flooding over the 21st Century. Sci. Rep. 10 (1), 1–12. https://doi.org/10.1038/s41598-020-67736-6.
Kobayashi, N., Raichle, A.W., Asano, T., 1993. Wave attenuation by vegetation. *Journal of waterway, port, coastal.* and ocean engineering 119 (1), 30–48.
Koch, E.W., Gust, G., 1999. Water flow in tide-and wave-dominated beds of the seagrass Thalassia testudinum. Mar. Ecol. Prog. Ser. 184, 63–72. https://doi.org/10.3354/meps184063.
Koftis, T., Prinos, P., Stratigaki, V., 2013. Wave damping over artificial Posidonia oceanica meadow: a large-scale experimental study. Coast. Eng. 73, 71–83. https://doi.org/10.1016/j.coastaleng.2012.10.007.
Komar, P.D., Miller, M.C., 1973. The threshold of sediment movement under oscillatory water waves. J. Sediment. Res. 43 (4). https://doi.org/10.1306/74d7290a-2b21-11d7-8648000102c1865d.
Leonard, L.A., Croft, A.L., 2006. The effect of standing biomass on flow velocity and turbulence in Spartina alterniflora canopies. Estuar. Coast Shelf Sci. 69 (3–4), 325–336. https://doi.org/10.1016/j.ecss.2006.05.004.
Losada, I.J., Maza, M., Lara, J.L., 2016. A new formulation for vegetation-induced damping under combined waves and currents. Coast. Eng. 107, 1–13. https://doi.org/10.1016/j.coastaleng.2015.09.011.
Lou, S., Chen, M., Ma, G., Liu, S., Wang, H., 2022. Sediment suspension affected by submerged rigid vegetation under waves, currents and combined wave–current flows. Coast. Eng. 173, 104082. https://doi.org/10.1016/j.coastaleng.2022.104082.
Lowe, R.J., Koseff, J.R., Monismith, S.G., 2005. Oscillatory flow through submerged canopies: 1. Velocity structure. J. Geophys. Res.: Oceans 110 (C10). https://doi.org/10.1029/2004JC002788.
Luhar, M., Nepf, H.M., 2016. Wave-induced dynamics of flexible blades. J. Fluid Struct. 61, 20–41. https://doi.org/10.1016/j.jfluidstructs.2015.11.007.
Luhar, M., Coutu, S., Infantes, E., Fox, S., Nepf, H., 2010. Wave-induced velocities inside a model seagrass bed. J. Geophys. Res.: Oceans 115 (C12). https://doi.org/10.1029/2010JC006345.
Luhar, M., Infantes, E., Nepf, H., 2017. Seagrass blade motion under waves and its impact on wave decay. J. Geophys. Res.: Oceans 122 (5), 3736–3752. https://doi.org/10.1002/2017JC012731.
Luijendijk, A., Hagenaars, G., Ranasinghe, R., Baart, F., Donchyts, G., Aarninkhof, S., 2018. The state of the world's beaches. Sci. Rep. 8 (1), 6641.
Marin-Diaz, B., Bouma, T.J., Infantes, E., 2020. Role of eelgrass on bed-load transport and sediment resuspension under oscillatory flow. Limnol. Oceangr. 65 (2), 426–436.
Masselink, G., Brown, T., Scott, T., Brodie, L., 2024. Sediment sorting within a relatively wave-exposed and sandy subtidal seagrass (Zostera marina) meadow. Mar. Geol. 476, 107385.
Mathisen, P.P., Madsen, O.S., 1996. Waves and currents over a fixed rippled bed: 1. Bottom roughness experienced by waves in the presence and absence of currents. J. Geophys. Res.: Oceans 101 (C7), 16533–16542. https://doi.org/10.1029/96jc00954.
Maza, M., Lara, J.L., Losada, I.J., Ondiviela, B., Trinogga, J., Bouma, T.J., 2015. Large-scale 3-D experiments of wave and current interaction with real vegetation. Part 2: experimental analysis. Coast. Eng. 106, 73–86. https://doi.org/10.1016/j.coastaleng.2015.09.010.
Mazda, Y., Magi, M., Ikeda, Y., Kurokawa, T., Asano, T., 2006. Wave reduction in a mangrove forest dominated by Sonneratia sp. Wetl. Ecol. Manag. 14, 365–378. https://doi.org/10.1007/s11273-005-5388-0.
McKee, K.L., 2011. Biophysical controls on accretion and elevation change in Caribbean mangrove ecosystems. Estuar. Coast Shelf Sci. 91 (4), 475–483. https://doi.org/10.1016/j.ecss.2010.05.001.
McKee, K.L., Cahoon, D.R., Feller, I.C., 2007. Caribbean mangroves adjust to rising sea level through biotic controls on change in soil elevation. Global Ecol. Biogeogr. 16 (5), 545–556. https://doi.org/10.1111/j.1466-8238.2007.00317.x.
Mcowen, C.J., Weatherdon, L.V., Van Bochove, J.W., Sullivan, E., Blyth, S., Zockler, C., Stanwell-Smith, D., Kingston, N., Martin, C.S., Spalding, M., Fletcher, S., 2017. A global map of saltmarshes. Biodivers. Data J. (5). https://doi.org/10.3897/BDJ.5.e11764.
Menéndez, P., Losada, I.J., Torres-Ortega, S., Narayan, S., Beck, M.W., 2020. The global flood protection benefits of mangroves. Sci. Rep. 10 (1), 1–12. https://doi.org/10.1038/s41598-020-61136-6.
Miller, M.C., Komar, P.D., 1980. A field investigation of the relationship between oscillation ripple spacing and the near-bottom water orbital motions. J. Sediment. Res. 50 (1), 183–191. https://doi.org/10.2110/jsr.50.183.
Möller, I., 2006. Quantifying saltmarsh vegetation and its effect on wave height dissipation: results from a UK East coast saltmarsh. Estuar. Coast Shelf Sci. 69 (3–4), 337–351. https://doi.org/10.1016/j.ecss.2006.05.003.
Möller, I., Kudella, M., Rupprecht, F., Spencer, T., Paul, M., Van Wesenbeeck, B.K., Wolters, G., Jensen, K., Bouma, T.J., Miranda-Lange, M., Schimmels, S., 2014. Wave attenuation over coastal salt marshes under storm surge conditions. Nat. Geosci. 7 (10), 727–731. https://doi.org/10.1038/ngeo2251.
Moritsch, M.M., Byrd, K.B., Davis, M., Good, A., Drexler, J.Z., Morris, J.T., Woo, I., Windham-Myers, L., Grossman, E., Nakai, G., Poppe, K.L., 2022. Can coastal habitats rise to the challenge? Resilience of estuarine habitats, carbon accumulation, and economic value to sea-level rise in a Puget Sound estuary. Estuaries Coasts 45 (8), 2293–2309. https://doi.org/10.1007/s12237-022-01087-5.
Mullarney, J.C., Henderson, S.M., Norris, B.K., Bryan, K.R., Fricke, A.T., Sandwell, D.R., Culling, D.P., 2017. A question of scale: how turbulence around aerial roots shapes the seabed morphology in mangrove forests of the Mekong Delta. Oceanography (Wash., D.C.) 30 (3), 34–47. https://doi.org/10.5670/oceanog.2017.312.
Narayan, S., Beck, M.W., Reguero, B.G., Losada, I.J., Van Wesenbeeck, B., Pontee, N., Sanchirico, J.N., Ingram, J.C., Lange, G.M., Burks-Copes, K.A., 2016. The effectiveness, costs and coastal protection benefits of natural and nature-based defences. PLoS One 11 (5), e0154735. https://doi.org/10.1371/journal.pone.0154735.
Nepf, H.M., Sullivan, J.A., Zavistoski, R.A., 1997. A model for diffusion within emergent vegetation. Limnol. Oceanogr. 42 (8), 1735–1745.
Nepf, H.M., 2012. Flow and transport in regions with aquatic vegetation. Annu. Rev. Fluid Mech. 44 (1), 123–142. https://doi.org/10.1146/annurev-fluid-120710-101048.
Nielsen, P., 1992. Coastal bottom boundary layers and sediment transport. World scientific 4. https://doi.org/10.1142/9789812796035.
Neumeier, U.R.S., Amos, C.L., 2006. The influence of vegetation on turbulence and flow velocities in European salt-marshes. Sedimentology 53 (2), 259–277.

Nielsen, P., 1986. Suspended sediment concentrations under waves. Coast. Eng. 10, 23–31. https://doi.org/10.1016/0378-3839(86)90037-2.
Norris, B.K., Mullarney, J.C., Bryan, K.R., Henderson, S.M., 2017. The effect of pneumatophore density on turbulence: a field study in a Sonneratia-dominated mangrove forest. Vietnam Continent. Shelf Res. 147, 114–127.
Norris, B.K., Mullarney, J.C., Bryan, K.R., Henderson, S.M., 2019. Turbulence within natural mangrove pneumatophore canopies. J. Geophys. Res.: Oceans 124 (4), 2263–2288. https://doi.org/10.1029/2018jc014562.
Norris, B.K., Mullarney, J.C., Bryan, K.R., Henderson, S.M., 2021. Relating millimeter-scale turbulence to meter-scale subtidal erosion and accretion across the fringe of a coastal mangrove forest. Earth Surf. Process. Landf. 46 (3), 573–592. https://doi.org/10.1002/esp.5047.
Ondiviela, B., Losada, I.J., Lara, J.L., Maza, M., Galván, C., Bouma, T.J., van Belzen, J., 2014. The role of seagrasses in coastal protection in a changing climate. Coast. Eng. 87, 158–168. https://doi.org/10.1016/j.coastaleng.2013.11.005.
Ozeren, Y., Wren, D.G., Wu, W., 2014. Experimental investigation of wave attenuation through model and live vegetation. J. Waterw. Port, Coast. Ocean Eng. 140 (5), 04014019. https://doi.org/10.1061/(ASCE)WW.1943-5460.0000259.
Pontee, N., Narayan, S., Beck, M.W., Hosking, A.H., 2016. Nature-based solutions: lessons from around the world. Proce. Institu. Civil Eng. Maritime Eng. 169 (1), 29–36. https://doi.org/10.1680/jmaen.15.00027. Thomas Telford Ltd.
Pujol, D., Serra, T., Colomer, J., Casamitjana, X., 2013. Flow structure in canopy models dominated by progressive waves. J. Hydrol. 486, 281–292. https://doi.org/10.1016/j.jhydrol.2013.01.024.
Quartel, S., Kroon, A., Augustinus, P.G.E.F., Van Santen, P., Tri, N.H., 2007. Wave attenuation in coastal mangroves in the red river delta, vietnam. J. Asian Earth Sci. 29 (4), 576–584. https://doi.org/10.1016/j.jseaes.2006.05.008.
Ranasinghe, R., 2016. Assessing climate change impacts on open sandy coasts: a review. Earth Sci. Rev. 160, 320–332. https://doi.org/10.1016/j.earscirev.2016.07.011.
Reidenbach, M.A., Thomas, E.L., 2018. Influence of the seagrass, Zostera marina, on wave attenuation and bed shear stress within a shallow coastal bay. Front. Mar. Sci. 5, 397. https://doi.org/10.3389/fmars.2018.00397.
Reidenbach, M.A., Timmerman, R., 2019. Interactive effects of seagrass and the microphytobenthos on sediment suspension within shallow coastal bays. Estuar. Coasts 42 (8), 2038–2053.
Reimann, L., Vafeidis, A.T., Honsel, L.E., 2023. Population development as a driver of coastal risk: current trends and future pathways. Cambridge Prisms: Coastal Futures 1, e14. https://doi.org/10.1017/cft.2023.3.
Ros, À., Colomer, J., Serra, T., Pujol, D., Soler, M., Casamitjana, X., 2014. Experimental observations on sediment resuspension within submerged model canopies under oscillatory flow. Cont. Shelf Res. 91, 220–231. https://doi.org/10.1016/j.csr.2014.10.004.
Seddon, N., Daniels, E., Davis, R., Chausson, A., Harris, R., Hou-Jones, X., Huq, S., Kapos, V., Mace, G.M., Rizvi, A.R., Reid, H., 2020. Global recognition of the importance of nature-based solutions to the impacts of climate change. Global Sustain. 3, e15. https://doi.org/10.1017/sus.2020.8.
Sleath, J.F., Wallbridge, S., 2002. Pickup from rippled beds in oscillatory flow. J. Waterw. Port, Coast. Ocean Eng. 128 (6), 228–237. https://doi.org/10.1061/(ASCE)0733-950X(2002)128:6(228).
Sumer, B.M., Christiansen, N., Fredsøe, J., 1997. The horseshoe vortex and vortex shedding around a vertical wall-mounted cylinder exposed to waves. J. Fluid Mech. 332, 41–70. https://doi.org/10.1017/s0022112096003898.
Sutton-Grier, A.E., Wowk, K., Bamford, H., 2015. Future of our coasts: the potential for natural and hybrid infrastructure to enhance the resilience of our coastal communities, economies and ecosystems. Environ. Sci. Pol. 51, 137–147. https://doi.org/10.1016/j.envsci.2015.04.006.
Swart, D.H., 1974. Offshore Sediment Transport and Equilibrium Beach Profiles, Publ. 131, Delft Hydraul. Lab., Delft, Netherlands.
Tang, C., Lei, J., Nepf, H.M., 2019. Impact of vegetation-generated turbulence on the critical, near-bed, wave-velocity for sediment resuspension. Water Resour. Res. 55 (7), 5904–5917. https://doi.org/10.1029/2018wr024335.
Tang, J., Chen, Y., Shen, Y., Cao, S., 2024. Numerical study on stem-generated turbulence due to emerged rigid vegetation in water waves. Ocean Eng. 304, 117940, 0.1016/j.oceaneng.2024.117940.
Temmerman, S., Meire, P., Bouma, T.J., Herman, P.M., Ysebaert, T., De Vriend, H.J., 2013. Ecosystem-based coastal defence in the face of global change. Nature 504 (7478), 79–83. https://doi.org/10.1038/nature12859.
Thielicke, W., Sonntag, R., 2021. Particle Image Velocimetry for MATLAB: Accuracy and enhanced algorithms in PIVlab.
Thorne, P.D., Davies, A.G., Bell, P.S., 2009. Observations and analysis of sediment diffusivity profiles over sandy rippled beds under waves. J. Geophys. Res.: Oceans 114 (C2). https://doi.org/10.1029/2008jc004944.
Thorne, P.D., Williams, J.J., Davies, A.G., 2002. Suspended sediments under waves measured in a large-scale flume facility. J. Geophys. Res.: Oceans 107 (C8), 1–4. https://doi.org/10.1029/2001JC000988.
Thorne, P.D., Davies, A.G., Williams, J.J., 2003. Measurement of near-bed intra-wave sediment entrainment above vortex ripples. J. Geophys. Res. 30 (20), 2028. https://doi.org/10.1029/2003GL018427.
Tinoco, R.O., Coco, G., 2014. Observations of the effect of emerged vegetation on sediment resuspension under unidirectional currents and waves. Earth Surf. Dyn. 2 (1), 83–96. https://doi.org/10.5194/esurf-2-83-2014.
Tinoco, R.O., Coco, G., 2018. Turbulence as the main driver of resuspension in oscillatory flow through vegetation. J. Geophys. Res.: Earth Surf. 123 (5), 891–904. https://doi.org/10.1002/2017jf004504.
Tseng, C.Y., Tinoco, R.O., 2021. A two-layer turbulence-based model to predict suspended sediment concentration in flows with aquatic vegetation. Geophys. Res. Lett. 48 (3), e2020GL091255. https://doi.org/10.1029/2020GL091255.
Tseng, C.Y., Tinoco, R.O., 2022. From substrate to surface: a turbulence-based model for gas transfer across sediment-water-air interfaces in vegetated streams. Water Res. Res. 58 (1), e2021WR030776.
van Rijn, L.C., 2007. Unified view of sediment transport by currents and waves. I: Initiation of motion, bed roughness, and bed-load transport. J. Hydraul. Eng. 133 (6), 649–667.
van Rijn, L.C., Nieuwjaar, M.W., van der Kaay, T., Nap, E., van Kampen, A., 1993. Transport of fine sands by currents and waves. J. Water. Port Coast. Ocean Eng. 119 (2), 123–143.
Van Veelen, T.J., Fairchild, T.P., Reeve, D.E., Karunarathna, H., 2020. Experimental study on vegetation flexibility as control parameter for wave damping and velocity structure. Coast. Eng. 157, 103648. https://doi.org/10.1016/j.coastaleng.2020.103648.
Vousdoukas, M.I., Ranasinghe, R., Mentaschi, L., Plomaritis, T.A., Athanasiou, P., Luijendijk, A., Feyen, L., 2020. Sandy coastlines under threat of erosion. Nat. Clim. Change 10 (3), 260–263. https://doi.org/10.1038/s41558-020-0697-0.
Vuik, V., Heo, H.Y.S., Zhu, Z., Borsje, B.W., Jonkman, S.N., 2018. Stem breakage of salt marsh vegetation under wave forcing: a field and model study. Estuar. Coast Shelf Sci. 200, 41–58. https://doi.org/10.1016/j.ecss.2017.09.028.
Ward, N.D., Megonigal, J.P., Bond-Lamberty, B., Bailey, V.L., Butman, D., Canuel, E.A., Diefenderfer, H., Ganju, N.K., Goñi, M.A., Graham, E.B., Hopkinson, C.S., 2020. Representing the function and sensitivity of coastal interfaces in Earth system models. Nat. Commun. 11 (1), 2458. https://doi.org/10.1038/s41467-020-16236-2.
Wheeler, B.W., White, M., Stahl-Timmins, W., Depledge, M.H., 2012. Does living by the coast improve health and wellbeing? Health Place 18 (5), 1198–1201. https://doi.org/10.1016/j.healthplace.2012.06.015.
Williams, P.B., Kemp, P.H., 1971. Initiation of ripples on flat sediment beds. J. Hydraul. Div. 97 (4), 505–522. https://doi.org/10.1061/jyceaj.0002932.
Yang, J.Q., Chung, H., Nepf, H.M., 2016. The onset of sediment transport in vegetated channels predicted by turbulent kinetic energy. Geophys. Res. Lett. 43 (21), 11–261. https://doi.org/10.1002/2016GL071092.
Yang, S.L., 1998. The role of scirpus marsh in attenuation of hydrodynamics and retention of fine sediment in the yangtze estuary. Estuar. Coast Shelf Sci. 47 (2), 227–233. https://doi.org/10.1006/ecss.1998.0348.
Zavistoski, R.A., 1994. *Hydrodynamic effects of surface piercing plants*. Doctoral dissertation, Massachusetts Institute of Technology.
Zhang, Y., Nepf, H., 2019. Wave-driven sediment resuspension within a model eelgrass meadow. J. Geophys. Res.: Earth Surf. 124 (4), 1035–1053. https://doi.org/10.1029/2018JF004984.
Zhang, Y., Tang, C., Nepf, H., 2018. Turbulent kinetic energy in submerged model canopies under oscillatory flow. Water Resour. Res. 54 (3), 1734–1750. https://doi.org/10.1002/2017wr021732.
Zhu, M., Zhu, G., Nurminen, L., Wu, T., Deng, J., Zhang, Y., Qin, B., Ventelä, A.M., 2015. The influence of macrophytes on sediment resuspension and the effect of associated nutrients in a shallow and large lake (Lake Taihu, China). PLoS One 10 (6), e0127915. https://doi.org/10.1371/journal.pone.0127915.